Escape of near-inertial waves trapped in strong fronts through wave-wave interactions

Mariona Claret,[a,b,c] Eric Kunze,[a] A. Tandon,[d] and A. Mahadevan[c]

[a] *NorthWest Research Associates, Seattle, WA, USA*

[b] *Cooperative Institute for Climate, Ocean, and Ecosystem Studies, University of Washington, Seattle, WA, USA*

[c] *Woods Hole Oceanographic Institution, Woods Hole, MA, USA*

[d] *Department of Mechanical Engineering and Department of Estuarine and Ocean Sciences, University of Massachusetts Dartmouth, Darmouth, MA, USA.*

Corresponding author: Mariona Claret, mclaret@nwra.com

ABSTRACT: Wind-generated inertial motions are refracted by geostrophic vorticity gradients to propagate into the stratified ocean interior as near-inertial waves that can be trapped in anticyclonic regions of ocean fronts and eddies as subinertial waves. Here, we explore a nonlinear wave-wave interaction mechanism by which subinertial near-inertial waves trapped in a sharp front (vorticity Rossby number Ro~-0.85, front gradient Froude number Fr~0.8) can escape as superinertial near-inertial waves. Inferences are drawn from spectral and cross-bispectral analyses of numerical solutions of a process-study ocean model configured to represent a two-dimensional baroclinic front. The model is forced with a wind impulse. The resulting near-inertial wave fields are analyzed over the ensuing five inertial periods as the waves radiate downward. Resonant wave-wave interactions provide a pathway for trapped subinertial wave energy to radiate out of the front as free superinertial waves. Nonlinear interactions represent a significant component of the near-inertial wave energy budget, only a factor-of-two smaller than dissipation. Escaping waves only occur for either large front vorticity Rossby number or large front gradient Froude number in the band constrained by $0 < 1 + \mathrm{Ro} - \mathrm{Fr}^2 < 0.36$.

1. Introduction

Wind-work powers 0.2 – 1.1 TW of surface-layer inertial oscillations globally (Plueddemann and Farrar 2006; Furuichi et al. 2008; Rimac et al. 2013; Jiang et al. 2005; Chaigneau et al. 2008; Alford 2020; Klenz et al. 2022, and references therein). These motions are transformed into near-inertial waves (NIWs) that propagate into the stratified ocean interior (e.g., Leaman 1976; Weller 1985; D'Asaro 1989; Niwa and Hibiya 1999; Silverthorne and Toole 2009; Alford et al. 2012; Cuypers et al. 2013; Pallàs-Sanz et al. 2016) by interactions with planetary β (Fu 1981; Gill 1984; D'Asaro 1989; D'Asaro et al. 1995; Garrett 2001) as well as with meso- and submesoscale vertical relative vorticity ζ gradients (Mooers 1975a,b; Weller 1982; Kunze 1985; D'Asaro 1995; Klein and Treguier 1993, 1995; Young and Ben Jelloul 1997; Klein et al. 2004; Danioux et al. 2008, 2011; Thomas et al. 2020; Asselin and Young 2020; Raja et al. 2022; Kunze et al. 2023) to form the near-inertial peak of the internal-wave frequency spectra in kinetic energy (Fu 1981; Polzin and Lvov 2011). Because vorticity refraction is typically 1-2 orders of magnitude larger than planetary β refraction (van Meurs 1998; Danioux et al. 2008; Asselin et al. 2020; Kunze et al. 2023), interactions with eddy vorticity exert the dominant control over where near-inertial waves propagate and dissipate. NIWs are thought to be one of the principal sources of turbulence production in the stratified ocean interior (Gregg et al. 1986; Kunze et al. 1990; Polzin 1996).

Vorticity refracts near-inertial waves out of regions of cyclonic and into anticyclonic vorticity (Kunze 1985; Danioux et al. 2008; Elipot et al. 2010; Asselin et al. 2020) so that near-inertial energy will tend to become trapped where the effective frequency $f_e = [f(f+\zeta)]^{1/2}$ is lower than the Coriolis frequency f (Perkins 1976; Mooers 1975a; Kunze 1985). If vorticity weakens with depth, as is typical for baroclinic mesoscale eddies and fronts, trapped downward-propagating near-inertial waves will stall and amplify at the base of anticyclonic regions at a vertical critical layer where the vertical wavelength and vertical group velocity shrink (Kunze 1985). Critical-layer amplification has been verified observationally (Kunze and Sanford 1984; Kunze 1986; Kunze et al. 1995; Joyce et al. 2013; Martínez-Marrero et al. 2019) and numerically (Wang 1991; Lee and Niiler 1998; Zhai et al. 2005; Claret and Viúdez 2010; Danioux et al. 2015; Lelong et al. 2016; Asselin and Young 2020).

Kunze et al. (1995) listed three possible sinks for this trapped near-inertial energy – (i) turbulent dissipation, (ii) wave-mean flow exchange, and (iii) wave-wave interaction exchange with super-

inertial internal waves free to radiate out of the anticyclonic trapping region. Elevated turbulent dissipation rates have been observed associated with elevated near-inertial shear in anticyclones (Lueck and Osborn 1986; Kunze et al. 1995; Kunze and Toole 1997). Elevated dissipation balanced trapped near-inertial wave energy-flux convergence, or wave pressure-work, in a Gulf Stream warm-core ring to within factor-of-two uncertainties (Kunze et al. 1995), making this the most likely sink. Wave-mean exchange can be ruled out as a major sink based on wave action E/ω_L conservation (Jones 1967), where ω_L is the Lagrangian or intrinsic frequency, since vortex-trapped wave frequencies remain close to f (Llewellyn Smith 1999).

With factor-of-two uncertainties in the dissipative sink (i), trapped near-inertial energy transferring to free waves that escape (iii) remains a possibility which is explored for the first time here using numerical simulations. Interaction of two trapped near-inertial waves with frequencies below f can generate a daughter wave with factor-of-two higher frequency that is free to propagate out of anticyclonic trapping region. The wave triads identified here do not fit into the three scale-separated cases identified by McComas and Bretherton (1977). However, recent work shows the importance of spectrally-local as well as scale-separated wave-wave interactions (Wu and Pan 2023; Dematteis et al. 2024).

Our investigations are made with an ocean model initialized with a strong (vorticity Rossby number $Ro = \zeta/f = -0.85$ and front gradient Froude number $Fr = |u_z|/N = 0.8$, where ζ and u_z are the front vertical relative vorticity and vertical shear, respectively) submesoscale front in thermal-wind balance, and forced with an initial 6-hour wind event that generates inertial currents at the surface (Sec. 2). Time evolution of the flow is analysed for five inertial periods after the wind event, documenting generation of NIWs, their downward radiation, followed by wave-trapping and amplification within the anticyclonic side of the front (Sec. 3). A total wave energy budget shows that wave-wave interactions represent sinks for wind-generated energy within the front (Sec. 4). Frequency and vertical wavenumber cross-bispectra show energy transfers from two pairs of trapped subinertial parent waves – one with the two frequencies centered at $0.8f$ and f, and the other with the two frequencies centered at $0.6f$ and $0.8f$ – to a superinertial wave of higher vertical wavenumber (Sec. 5). Resonant wave-triad escape only occurs from trapping regions where $0 < 1 + Ro - Fr^2 < 0.36$. Finally, Sec. 6 offers a summary, implications of this nonlinear mechanism in the ocean and suggestions for future work.

2. Numerical modeling

a. Process Ocean Study Model

The Process Study Ocean Model (PSOM) is a non-hydrostatic, free-surface numerical model that simulates the flow of a stratified rotating fluid under the Boussinesq approximation (Mahadevan et al. 1996a,b). This model is fully three-dimensional and has been used previously to examine spontaneous generation and propagation of IGWs by a meandering front (Nagai et al. 2015). Here, the model is configured to simulate a 2-D geostrophic front with propagation of surface-generated near-inertial waves in the vertical and cross-front directions. This simple scenario allows us to focus on depth propagation and interactions of NIWs generated near the surface.

b. Model domain and boundary conditions

The domain is a periodic zonal along-jet channel with no-flux boundary conditions to the north and south. The bottom is also a no-flux solid boundary, while the top boundary is a free surface. The zonal domain extent is $L_X = 6.4\,\mathrm{km}$, meridional $L_Y = 148\,\mathrm{km}$, and depth $L_Z = 422\,\mathrm{m}$. The limited zonal extent prevents baroclinic instability and along-front wave propagation so that the simulation is effectively 2-D. Using $N_X \times N_Y \times N_Z = 16 \times 371 \times 136$ grid points (excluding sponge and buffer layers, see details below), the lateral resolution of the grid is $\Delta x = \Delta y = 400\,\mathrm{m}$, while the vertical resolution ranges from $\Delta z = 2.3\,\mathrm{m}$ near the surface to $4.2\,\mathrm{m}$ at $z = -L_Z$. Therefore, waves with minimum horizontal and vertical wavelengths of $800\,\mathrm{m}$ and $8.4\,\mathrm{m}$, respectively, and an aspect ratio of about 0.01, are fully resolved. The time step $\Delta t = 90\,\mathrm{s}$ is appropriate for resolving waves with periods ranging from the inertial period to hours, which are typical of inertia–gravity waves (Garrett and Munk 1979).

To simulate radiation into the deeper ocean, a bottom wave-absorbing layer is implemented that minimizes reflections back into the water column with Rayleigh damping $\mathbf{R}$ added to the right-hand side of the momentum equations of the form $\mathbf{R}(\mathbf{x},t) = -r(z)\,\mathbf{u}(\mathbf{x},t)$ (Durran 1998), where $r(z)$ is a vertically dependent relaxation rate, and $\mathbf{u}(\mathbf{x},t) = (u,v,w)$ the three-dimensional velocity vector. The sponge layer scheme is similar to that in MITgcm (Zhang and Marotzke 1999; Grisouard 2010), $r(z) = (1-s(z))/[(1-s(z))\Gamma_\mathrm{o} + s(z)\Gamma_\mathrm{i}]$, where $s(z)$ is the distance from the bottom boundary in grid points normalized by the 120 points within the sponge layer. In this way, velocities gradually relax to zero over a timescale Γ_i at the inner edge and Γ_o at the bottom. We set $\Gamma_\mathrm{i} = 4\,\mathrm{T_{ip}}$ and

$\Gamma_o = \Gamma_i/1000$, where T_{ip} is one inertial period, which is the upper bound of the time period range of IGWs.

c. Subgrid-scale damping

Laplacian momentum and buoyancy damping are included with uniform lateral eddy viscosity and diffusivity $\kappa_h = 1\,\mathrm{m^2\,s^{-1}}$. When winds are turned on, the vertical viscosity and diffusivity κ_v have a prescribed profile $\kappa_v(z) = \max\left\{\kappa_v^{\min}, \kappa_v^{\max} 0.5\left[1+\tanh\left\{(z-z_m)/z_m 2\pi\right\}\right]\right\}$, where $z_m = -40\,\mathrm{m}$ is the mixing-layer depth at which κ_v decays from $\kappa_v^{\max} = 10^{-2}\,\mathrm{m^2\,s^{-1}}$ to $\kappa_v^{\min} = 10^{-4}\,\mathrm{m^2\,s^{-1}}$ (Dewey and Moum 1990). In the absence of winds, κ_v is uniform with value $\kappa_v^{\min}$. Wind-generated inertial oscillations are initially confined to the mixing layer. Sensitivity to other diffusivities is also tested (Appendix A).

d. Front initialization

The model is initialized with an idealized density front and jet in geostrophic balance. The initial buoyancy distribution $b(y,z) = b_0 + N_0^2 z + b_f(y,z)$ is comprised of a constant buoyancy $b_0 = -g$, where g is the acceleration due to gravity, a linear density stratification $N_0^2 = 9.6\times10^{-6}\,\mathrm{rad^2\,s^{-2}}$ and a front buoyancy anomaly $b_f(y,z) = -g/\rho_0\left[\tanh\left\{\pi\left(z_f(y)-z\right)/\Delta Z\right\}+1\right]/2$, where $\rho_0 = 1025.8\,\mathrm{kg/m^3}$ and $\Delta Z = 175\,\mathrm{m}$ is the vertical front extent. The front mid-depth varies laterally as $z_f(y) = Z_0\left[\tanh\left\{2\pi\left(y-Y_0\right)/\Delta Y\right\}-1\right]/2$, where $\Delta Y = 57\,\mathrm{km}$ is the width of the front centered at Y_0, $Z_0 = H + \Delta Z/2$, and $H = 50\,\mathrm{m}$ the depth of the surface layer on the buoyant side of the front (see Fig. 1a). Parameters ΔZ, ΔY, and H are empirically constrained using Gulf Stream observations from the Line W program (www.whoi.edu/science/PO/linew) to represent a front typical of a western boundary current.

The front has maximum buoyancy frequency $N = 10^{-2}\,\mathrm{rad\,s^{-1}}$, defined by $N^2 \equiv b_z$ where subscript z is the partial derivative with respect to the vertical, which is deepest on the buoyant side of the front and shoals toward the denser side (Fig. 1b). The strongest lateral buoyancy gradient $-6.19\times10^{-7}\,\mathrm{s^{-2}}$ results in a maximum geostrophically balanced velocity of $0.82\,\mathrm{m\,s^{-1}}$ for a mean latitude of $35°N$. The geostrophic relative vertical vorticity ζ_g attains maximum and minimum values of $0.99f$ and $-0.85f$, respectively, where f is the Coriolis frequency. The resulting initial baroclinic front has a minimum Richardson number $Ri \equiv N^2/u_z^2 = 1.5$, corresponding to a maximum gradient Froude

number $Fr \equiv |u_z|/N = 0.8$ (Fig. 1c). Although isopycnals are steep, the front is symmetrically stable initially since the 2D Ertel's geostrophic potential vorticity q_g, defined as $q_g \equiv f(f+\zeta_g)b_z - b_y^2$, where subscript y is the partial derivative with respect to the meridional coordinate, is positive everywhere (Hoskins 1974).

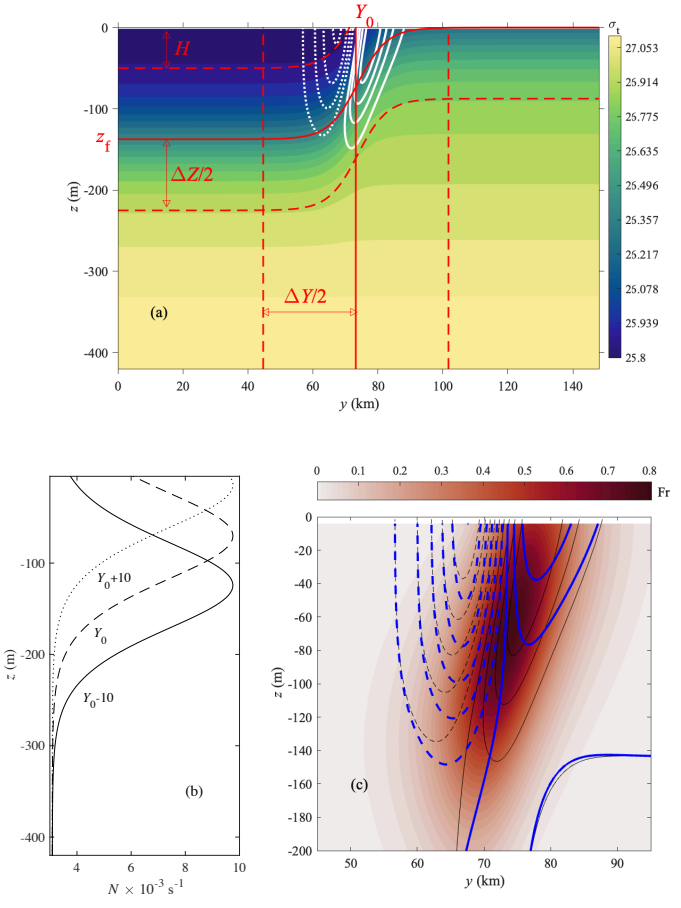

FIG. 1. (a) Cross-section of initial frontal density (shading) and vorticity (white contours every $0.2f$, solid positive vorticity, dashed negative vorticity) structure representative of the Gulf Stream. The jet is out of the page and in geostrophic balance. Initial density structure is an analytical function (see text) that depends on four parameters: front width ΔY, front vertical extent ΔZ, thickness of a homogeneous surface layer H, and front center Y_0. (b) Buoyancy stratification N profiles in the center of the jet (dashed), and on its anticyclonic (solid) and cyclonic (dotted) sides, 10 km from the center. (c) Gradient Froude number across the front (shading), effective inertial frequency f_e (thin black contours) and $\omega_{\min}$ (thick blue contours), both with contour intervals of $0.1f$ and dashed/solid lines for frequencies below/above f. Gradient Froude numbers are larger on the cyclonic ($f_e > f$) side of the front.

e. Inertial motions

The model is impulsively forced with a cross-front wind-stress $\tau = 0.26$ Pa during the first six hours. This is a simple way to generate free inertial oscillations in the upper layer because the ocean resonates at the inertial frequency after the wind stops (e.g., Ekman 1905). The resulting inertial motions have the same order of magnitude as the initial geostrophic current, with maximal velocities of about 0.3 m s^{-1} at the surface decaying to 0 at the base of the mixing layer. Since we are interested in post-generation evolution of these inertial motions, we hereafter refer to $t = 0$ as the time when the wind is turned off.

Because the wind-stress τ is applied perpendicular to the front, there is no wind-work on the geostrophic flow, since $\kappa_v \partial v/\partial z = -\tau/f$, where κ_v is the vertical eddy viscosity. The wind-stress is uniform over the front, but tapers gradually to zero near the solid lateral boundaries. The buffer region is 200 grid points wide. The grid spacing in this region increases gradually from 400 m to as much as 10 km so as to weaken the wind-stress curl, and minimize inertial pumping (Gill 1984).

3. Downward propagation of superinertial waves

Time evolution of wind-generated inertial motions during the first five inertial periods T_{ip} after cessation of the wind is described. To distinguish between the front (mean) and waves, signals are decomposed into a time-mean computed over 5 T_{ip} and a perturbation

$$\mathbf{u} = \bar{\mathbf{u}} + \mathbf{u}', \quad p = \bar{p} + p', \quad b = \bar{b} + b', \quad \zeta = \bar{\zeta} + \zeta', \tag{1}$$

where overbars and primes denote the time-mean and fluctuating components of the velocity vector $\mathbf{u} = (u, v, w)$, pressure p, buoyancy b and vertical relative vorticity ζ. Other wave-mean flow decompositions have been explored since a frequency continuum is excited which may not be fully captured in the perturbation component. As shown in Sec. 4, the wave energy budget is relatively insensitive to time-means ranging over 4.5-5.5 T_{ip} after the wind impulse, or as the front initial condition.

The initial post-wind state is dominated by a coherent slab of cross-front velocity v' in the mixing layer (Fig. 2a), which extends to approximately 35-m depth. At later times, v' dephases across the

front and tilted bands of alternating v' form in the interior (Fig. 2b). These motions are strongest and have the smallest vertical scales in the anticyclonic vorticity (Fig. 2c).

Away from the front, the upper ocean rings at the inertial frequency. Within the front, this ringing is modulated by relative vorticity (Klein et al. 2004) so that the intrinsic frequency of wind-generated waves is shifted from f to an effective inertial frequency f_e, where $f_e^2 \equiv f(f+\bar{\zeta}) = f^2(1+\overline{Ro})$ (Mooers 1975a; Weller 1982; Kunze 1985; Young and Ben Jelloul 1997; Asselin and Young 2020), and $Ro \equiv \zeta/f$ is the Rossby number. The resulting near-inertial waves rapidly radiate downward and can propagate freely as wave packets in regions where the lower bound of the internal-wave frequency band $\omega_{\min}$ lies below the wave frequency ω but not where $\omega_{\min}$ exceeds ω, with $\omega_{\min}^2 = f_e^2 - \bar{b}_y^2/\bar{b}_z = f^2(1+\overline{Ro}-\overline{Fr}^2)$ the lowest bound of the frequency range of inertia–gravity waves propagating through flows with front Rossby and gradient Froude numbers of $O(1)$ (Mooers 1975a,b; Kunze 1985; Whitt and Thomas 2013). Considering the gradient Froude number of the mean-flow $\overline{Fr} \equiv |\bar{u}_z|/\bar{N} = |\bar{b}_y|/f\bar{N}$, where $f\bar{u}_z = -\bar{b}_y$ is the mean-flow thermal-wind balance, the region where subinertial waves are trapped and wave energy accumulates is enlarged compared to that only considering f_e as a result of baroclinicity $\bar{b}_y$ (Fig. 1c) where the trapping region on the anticyclonic frontal side is defined by $f\bar{\zeta} - \bar{b}_y^2/\bar{b}_z = f^2(\overline{Ro}-\overline{Fr}^2) < 0$.

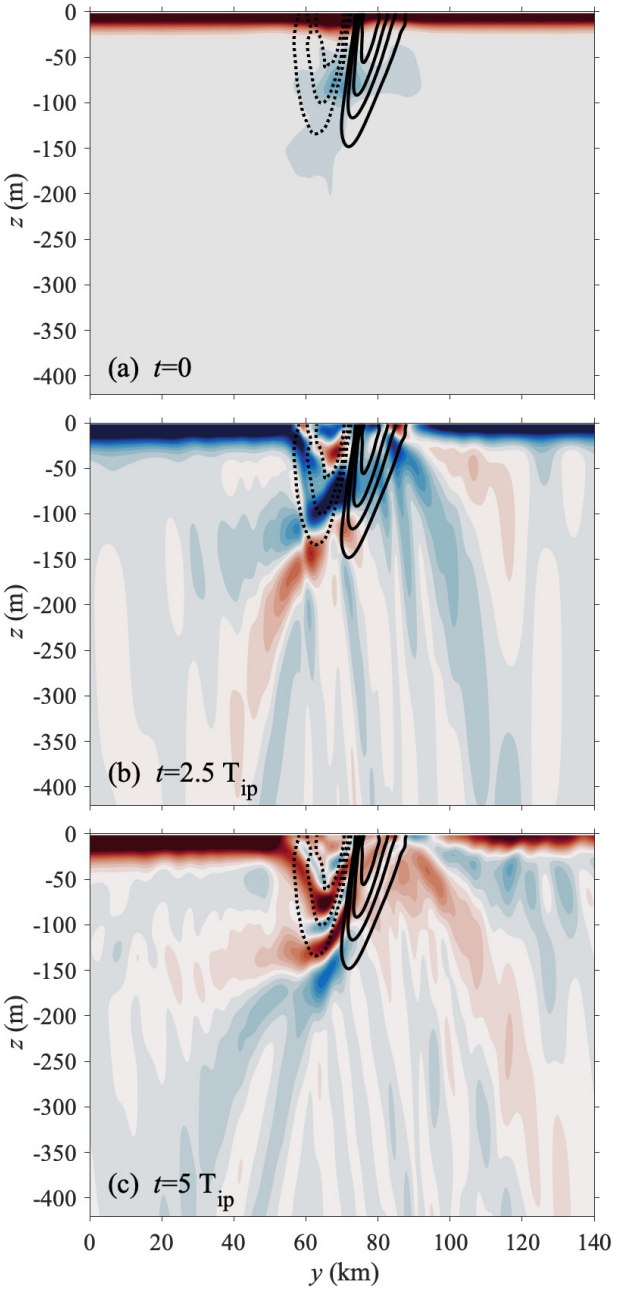

FIG. 2. Perturbation cross-front velocity v' at $t = 0$ (a), $t = 2.5\ \mathrm{T_{ip}}$ (b), and $t = 5\ \mathrm{T_{ip}}$ (c) inertial periods after the wind is turned off. At $t = 0$, v' is strongest in the mixing layer and points in the same direction at all cross-front locations. At later times, it is banded vertically and across-front beneath the mixing layer. The bands have the largest magnitudes at the base of the anticyclonic side of the front. Relative vertical vorticity contours of the mean-flow are included for reference with contour interval of $0.2f$ and with dashed (solid) lines for negative (positive) values.

Depth-binned frequency spectra of perturbation horizontal velocity show a prominent peak at f within the mixing layer (Fig. 3, black line) due to the dominance of inertial motions generated by wind forcing. Below this layer within the front, this inertial peak decays and broadens towards both subinertial and superinertial frequencies, in agreement with modulation by $\bar{\zeta}$ of the intrinsic frequency and rapid downward wave propagation (Fig. 3, red line). Below the front, superinertial waves become relatively more important (Fig. 3, blue line), consistent with subinertial waves being trapped in the front and nonlinear transfer of wave energy out of the inertial peak.

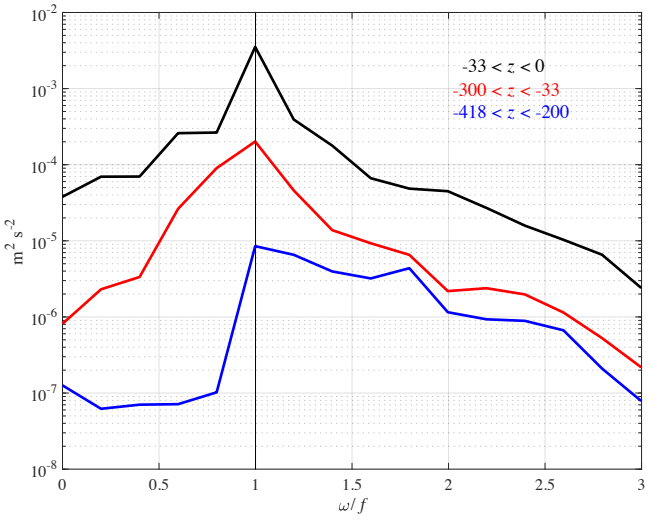

FIG. 3. Laterally-averaged depth-binned frequency power spectra of horizontal velocity (u',v') in the mixing layer $z > -33$ m (black curve), over front depths $-300 < z < -33$ m (red curve), and below the front $-418 < z < -200$ m (blue curve) using a Tukey window of 15%. The inertial frequency is indicated by a solid vertical line. At mid-depth (red), the inertial peak broadens toward subinertial frequencies, a signature of trapped near-inertial waves. Below the front (blue), superinertial waves are relatively more important.

To gain further insights on the wave frequency spatial distribution, we examine a cross-front section of the dominant frequency (that associated with the largest spectral amplitude) at each grid cell in the model. Subinertial frequencies are localized within the anticyclonic side of the front enclosed by contours of $\omega = \omega_{\min}$, while superinertial frequencies emanate as beams that align with IGW characteristics (Fig. 4). For instance, slopes of beams with $\omega = 1.4f$ and $\omega = 1.8f$ (see Fig. 4) are consistent with those predicted by the quiescent ocean dispersion relation $\ell/m = \pm\sqrt{(f^2-\omega^2)/(\omega^2-N_0^2)}$, where ℓ and m are cross-front and vertical wavenumbers, within 10% error. These wave beams originate near the anticyclonic side of the front and their wave

intrinsic frequencies are close to twice the dominant subinertial frequency $\omega = 0.8f$ within the anticyclonic region, suggesting generation by wave-wave interactions.

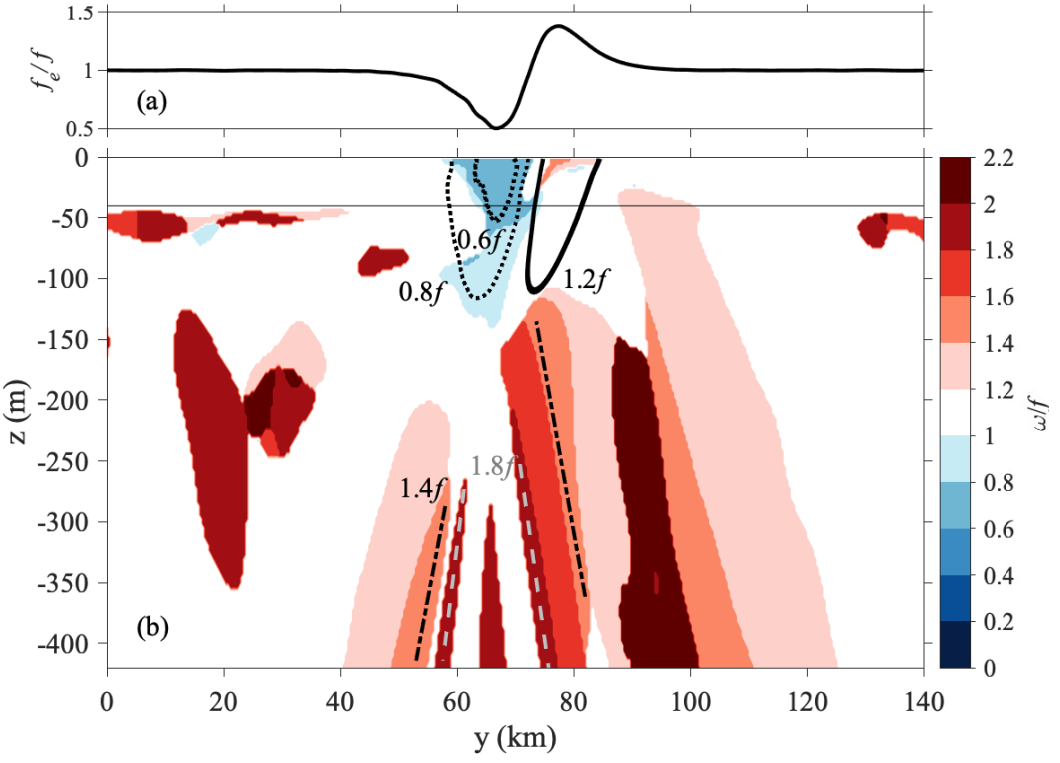

FIG. 4. (a) Cross-front distribution of f_e normalized by f at the surface. (b) Vertical section of the dominant wave frequency in the rotary spectra of $u' + iv'$ at each grid point over 5 Tip after the wind impulse (shading) and contours of $\omega_{\min} = (0.6f, 0.8f)$ on the anticyclonic side of the front (dotted contours) and $f_e = 1.2f$ on the cyclonic side (solid contours). Diagonal lines below 150-m depth indicate wave characteristic slopes for $\omega = 1.8f$ (dashed lines) and $\omega = 1.4f$ (dash-dotted lines), consistent with the corresponding beam frequencies. These beams have about twice the frequency of trapped subinertial waves on the anticyclonic side of the front below the mixing layer which can be greater than f_e, suggesting that they may be the result of wave-wave interactions. Mixing-layer depth is indicated by the thin horizontal line.

Construction of our model minimizes lateral Doppler-shifting because along-front wave phase gradients vanish ($k \times \bar{u} = 0$) and the mean cross-front velocity $\bar{v}$ is weak. An upper bound of the cross-front Doppler-shift based on the mean cross-front velocity ($\bar{v} = 8 \times 10^{-3}$ m s^{-1}) and minimum cross-front wavelength ($\lambda_y = 20$ km, Fig. 2) is $\ell \times \bar{v} = 0.035f$, one order-of-magnitude smaller than inferred frequency shifts. Vertical Doppler-shifting is also small although non-negligible with a

maximum value of $m \times \bar{w} = 0.13f$ from a maximum mean vertical velocity ($\bar{w} = 8.4 \times 10^{-5}$ m s^{-1}) and a minimum vertical wavelength ($\lambda_z = 50$ m, Fig. 2).

4. Wave energy budget

The wave energy equation is derived from non-hydrostatic momentum conservation, mass conservation and continuity. Retaining terms that involve wave-front and wave-wave interactions, the equations of motion under the Boussinesq approximation are

$$\frac{\partial \mathbf{u}'}{\partial t} + \bar{\mathbf{u}} \cdot \nabla \mathbf{u}' + \mathbf{u}' \cdot \nabla \bar{\mathbf{u}} + \mathbf{u}' \cdot \nabla \mathbf{u}' + f\mathbf{k} \times \mathbf{u}' = -\frac{1}{\rho_0} \nabla p' + b'\mathbf{k} + \mathcal{D}(\mathbf{u}'), \tag{2}$$

$$\frac{\partial b'}{\partial t} + \bar{\mathbf{u}} \cdot \nabla b' + \mathbf{u}' \cdot \nabla b' + \mathbf{u}' \cdot \nabla \bar{b} = \mathcal{D}(b') \tag{3}$$

$$\nabla \cdot \mathbf{u}' = 0, \tag{4}$$

where $\mathcal{D}(\cdot) = \kappa_h \nabla^2(\cdot) + \partial_z \kappa_v (\partial_z(\cdot))$, ∇_h^2 is the horizontal Laplacian operator, and ∂_z is the partial derivative with respect to z. Terms involving wave-front interactions are simplified because Doppler-shifting of the wave by the front is minimal and along-front gradients $\partial/\partial x$ of the front and waves vanish. An equation for the terms contributing to total wave energy $E' \equiv 1/2\,(|\mathbf{u}'|^2 + b'^2/N^2)$ at $t = 5$ T$_{\text{ip}}$ is obtained by multiplying (2) by the wave velocity vector and (3) by b'/N^2, adding terms, integrating over x $\langle(\cdot)\rangle$ and time to 5 T$_{\text{ip}}$

$$\begin{aligned}\langle E' \rangle = & \underbrace{-\int_0^{5\mathrm{T_{ip}}} \left(\langle u'v' \frac{\partial \bar{u}}{\partial y} \rangle + \langle u'w' \frac{\partial \bar{u}}{\partial z} \rangle \right) \mathrm{d}t}_{\text{MSP}} \underbrace{- \int_0^{5\mathrm{T_{ip}}} \langle \frac{v'b'}{N^2} \frac{\partial \bar{b}}{\partial y} \rangle \,\mathrm{d}t}_{\text{LBF}} \underbrace{- \int_0^{5\mathrm{T_{ip}}} \langle \mathbf{u}' \cdot \mathbf{u}' \cdot \nabla \mathbf{u}' \rangle \,\mathrm{d}t}_{\text{WWI}} \\ & \underbrace{- \int_0^{5\mathrm{T_{ip}}} \frac{1}{\rho_0} \langle \nabla \cdot (p'\mathbf{u}') \rangle \,\mathrm{d}t}_{\text{WPW}} \underbrace{+ \int_0^{5\mathrm{T_{ip}}} \langle \mathbf{u}' \cdot \mathcal{D}(\mathbf{u}') \rangle \,\mathrm{d}t + \int_0^{5\mathrm{T_{ip}}} \langle \frac{b'}{N^2} \mathcal{D}(b') \rangle \,\mathrm{d}t}_{\text{DIS}} + \text{s.m.t.}\end{aligned} \tag{5}$$

The five terms on the RHS include mean-flow shear production (MSP), cross-front wave buoyancy-flux (LBF), wave-wave interactions (WWI), wave pressure-work (WPW) and numerical dissipation (DIS). Nonlinear terms involving $\bar{\mathbf{u}} \cdot \nabla \mathbf{u}'$, $\bar{\mathbf{u}} \cdot \nabla b'$ and $\mathbf{u}' \cdot \nabla b'$ are included in (5) as small-magnitude terms (s.m.t.) to close the budget. Finally, the wave energy equation is integrated over the cross-front domain (142 km, see Fig. 1) to quantify the net contribution of each term to wave energy evolution below the mixing layer.

The dominant balance in the energy budget (Eq. 5) is between accumulation of wave energy (LHS) and wave pressure-work (WPW), indicating that the simulation has not achieved a later state where energy accumulation is overtaken by dissipation. The positive contribution of WPW to $\langle E' \rangle$ across the front (blue line in Fig. 5) signifies that there is convergence of energy-flux $\mathbf{F} = \langle p'\mathbf{u}' \rangle = \mathbf{c}E$, where $\mathbf{c}$ is the wave group velocity vector. Energy-flux convergence is consistent with downward propagation of the wind-generated wave energy pulse from the mixing layer boosting wave energy in the interior (Fig. 2). Further energy-flux convergence (WPW> 0) will amplify the wave pulse since it cannot leave the anticyclonic trapping region but will stall at a critical layer (Kunze and Sanford 1984; Kunze 1985; Kunze et al. 1995). The increase in total wave energy below the mixing layer to z =-180 m ($\sim$ 65% of WPW) is smaller than the WPW term due to non-negligible wave energy sinks arising from (i) dissipation (21.9%), (ii) wave-wave (9.0 ± 0.2% among the different wave-front decompositions) and (iii) wave-front (2.3 ± 1.0%) interactions, as well as (iv) a small contribution from s.m.t. (1%) that together close the budget [(5), Fig. 5]. Wave-front (MSP + LBF, comprising the Eliassen-Palm flux) energy exchanges are a wave source immediately below the mixing layer and a wave sink at greater depths (green curve in Fig. 5). Spontaneous IGW generation (Nagai et al. 2015; Shakespeare and Taylor 2016) is not expected here because the front is not unstable. In contrast, measurements in Gulf Stream warm-core rings find that dissipation balances wave pressure-work within factor-of-two measurement uncertainties (Kunze et al. 1995; Alford et al. 2025) which suggests steady state balance between wave pressure-work and dissipation in these ocean eddies.

Similar nonlinear energy transfers were reported by Silverthorne (2010) for a wind-forced scenario in a primitive-equation ocean model. The author reported that terms of the form $u'\langle \mathbf{u} \cdot \boldsymbol{\nabla} u \rangle + v'\langle \mathbf{u} \cdot \boldsymbol{\nabla} v \rangle$ in the 16-30 h period band were non-zero when integrated over the anticyclonic side of the front (Figs. 5-10). However, the separate contribution of wave-wave interactions to the wave kinetic energy in that case is unclear since nonlinear terms in Silverthorne (2010) included contributions from wave-front interactions.

In the remainder of this paper, the dynamics of the energy loss associated with the WWI term is explored in detail since it is novel to the best of our knowledge. While the effect of exchange between the front and near-inertial waves is of potential interest, this term is small, as expected since the absence of Doppler-shift $\mathbf{k} \cdot \bar{\mathbf{u}}$ implies that wave action $E/(\omega - \mathbf{k} \cdot \bar{\mathbf{u}})$ conservation is

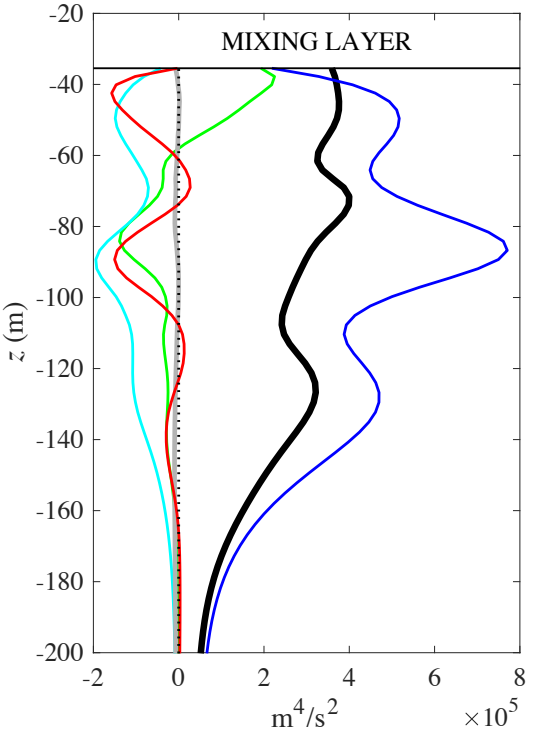

FIG. 5. Wave energy budget integrated over the model lateral domain and 5 T_{ip}. The black line is the total accumulated wave energy $\langle E' \rangle$, blue line pressure-work WPW, cyan line dissipation DIS plus small magnitude terms (s.m.t.), red line wave-wave interactions WWI, green line wave-front interactions term MSP+LBF, and the gray line the residual. The dotted vertical line is zero.

equivalent to wave energy conservation. Furthermore, it is not reliably quantified due to the short duration of our simulations.

5. Wave escape through resonant triads

In this section, the escape of trapped near-inertial wave energy from the anticyclonic trapping region as superinertial internal waves will be demonstrated. Resonant wave-wave triad interactions inside the trapping region allow more superinertial energy to leave than enter. Cross-bispectra identify the frequencies ω and vertical wavenumbers m of the parent waves from which one can infer the across-front wavenumbers ℓ of the parent waves using the front near-inertial wave dispersion relation (6). Assuming that the daughter wave has frequency $\omega_3 = \omega_1 + \omega_2 > f$ and vertical wavenumber $m_3 = m_1 + m_2$, one then determines which cross-front wavenumbers $\ell_3 = \ell_1 + \ell_2$

satisfies either the front

$$\omega^2 = f_e^2 - 2\bar{b}_y \frac{\ell}{m} + N_0^2 \frac{\ell^2}{m^2} \tag{6}$$

or quiescent ocean dispersion relation

$$\omega^2 = f_e^2 + N_0^2 \frac{\ell^2}{m^2} \tag{7}$$

as well as $\omega(\ell_3, m_3) = \omega_1 + \omega_2$ to produce a free wave; in practice, we require ω_3 from (6) or (7) to be within 15% of $\omega_1 + \omega_2$ to be considered a resonant interaction.

a. Energy-fluxes

Energy-flux convergence, or wave pressure-work (WPW), of trapped wind-generated downward-propagating subinertial wave energy occurs on the anticyclonic side of the front (Fig. 6a). At some locations (e.g., $y \simeq 63\,\mathrm{km}$), wave-wave interactions can be as large as the pressure-work (Fig. 6b) but, integrated across the front, WWI is smaller because it can act as both a source or sink depending on location.

Frequency analysis suggests radiation of superinertial wave beams with approximately twice the trapped near-inertial frequencies from the anticyclonic side of the front (Fig. 4). To quantify the subinertial [$\omega \in (0.4f, 0.8f)$, trapped], and superinertial [$\omega \in (1.4f, 1.8f)$] wave energy-flux into and out of the trapping region, band-passed wave pressure p'_b and velocity $\mathbf{u}'_b$ are used to compute a band-passed wave energy-flux $\mathbf{F}_b = \langle \mathbf{u}'_b p'_b \rangle / \rho_0$ integrated over $5\mathrm{T_{ip}}$ along the $\omega_{\min} = 0.96f$ perimeter below the mixing layer (gray contours in Fig. 6), with inward defined negative and outward positive.

Along the base of the mixing layer, both $\omega \in (0.4, 0.8)f$ and $\omega \in (1.4, 1.8)f$ energy-fluxes are mostly into the anticyclonic region (Fig. 7) while, along the bowl-shaped part of the perimeter in the pycnocline, subinertial energy-fluxes are weakly into the trapping region but superinertial energy-fluxes are out of the domain and 4% larger than inward fluxes, suggesting wave frequency transformations inside the anticyclonic trapping region. Outgoing superinertial energy-fluxes are largest close to the middle of the jet where the front gradient Froude number is the largest (Fig. 1c), suggesting that the $\omega = 1.4f$ and $\omega = 1.8f$ beams in Fig. 4 likely radiate from the jet's center.

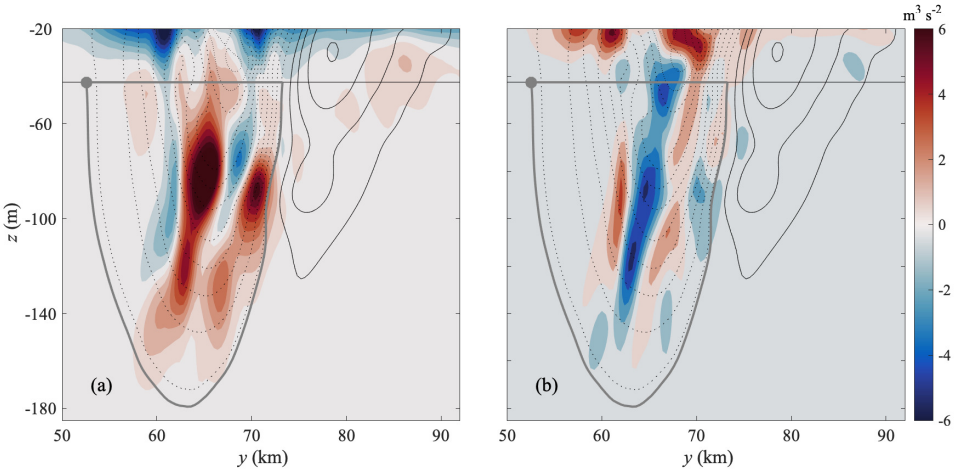

FIG. 6. Cross-front sections of (a) wave pressure-work WPW and (b) wave-wave interactions WWI (shadings). Positive and negative values are energy sources and sinks, respectively. Contours of $\omega_{\min}$ at $0.05f$ intervals are shown. The contour $\omega_{\min} = 0.96f$ along which WWI and WPW are integrated clockwise from the gray dot is indicated (thick gray line). Mixing-layer depth is the thin horizontal line.

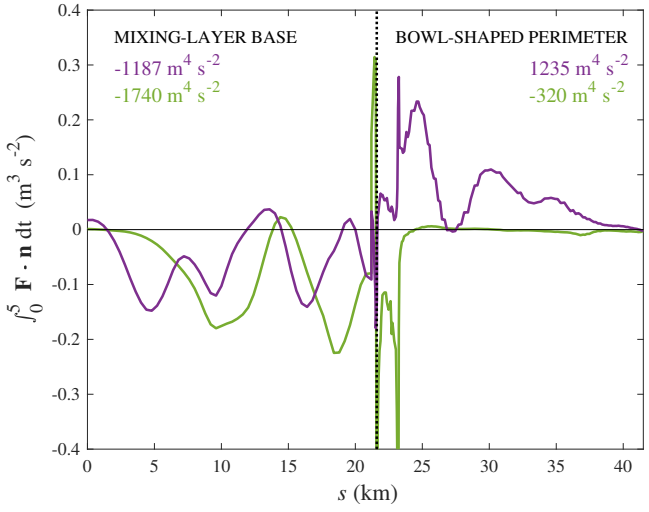

FIG. 7. Energy-fluxes through the $\omega_{\min} = 0.96f$ perimeter for subinertial frequencies $\omega \in (0.4f, 0.8f)$ (green) and superinertial frequencies $\omega \in (1.4f, 1.8f)$ (purple) integrated over $5\,T_{ip}$. The unit vector normal to the perimeter $\mathbf{n}$ is positive outwards. Curves to the left of dotted vertical line are along the base of the mixing layer and mostly inward for both frequency bands. Curves to the right of dotted line are along the anticyclonic bowl in the pycnocline and outward for the superinertial band. Perimeter-integrated energy-fluxes across both regions are indicated for both frequency passbands. Distance s is clockwise around the perimeter relative to the gray dot in Fig. 6.

b. Wave-wave interactions

Wave-wave interactions [WWI in (5)] integrated inside the $\omega_{\min} = 0.96f$ contour correspond to about 10% of the wave pressure-work (WPW). Cross-bispectra (Hinich and Clay 1968; Kim and Powers 1979) have been successfully applied to describe resonant interactions in the ocean (e.g., McComas and Briscoe 1980; Niwa and Hibiya 1997; Furue 2003; Furuichi et al. 2005; Williams et al. 2006; Carter and Gregg 2006; MacKinnon et al. 2013; Sun and Pinkel 2013; Skitka et al. 2024) and are used here to identify wave frequencies ω and vertical wavenumbers m for the interacting waves. The reader is referred to Appendix B for a detailed definition of the cross-bispectrum, its physical interpretation and the relation between the cross-bispectra constructed here and wave triplets in the WWI term.

Nonlinear wave triplets are decomposed in frequency inside the $\omega_{\min} = 0.96f$ contour (gray curve in Fig. 6b) and in vertical wavenumber on the anticyclonic side of the front. Four triplets dominate contributions to WWI: $u'v'u'_y$, $u'w'u'_z$, $v'v'v'_y$ and $v'w'v'_z$ (Fig. B1). Although triplets involving lateral shears have smaller net contributions, they are included since they can be as large as the other two triplets at some gridpoints (not shown). Wave properties are first WKB-scaled (Leaman and Sanford 1975) using (B6–B7) to remove variability due to changes in stratification. This WKB normalization gives cleaner cross-bispectral estimates (not shown). Cross-bispectral values are tested against ensemble averages of triple products associated with wave energy transfers following (B15) and (B18)–(B20) to provide verification. Given that nonlinear interactions in this simulation may be more heterogeneous and nonstationary than assumed by the underlying statistical uncertainty analysis, 95% confidence limits are estimated using time series (vertical profiles) where the phase of the first property in triplets is arbitrarily shifted (details in Appendix B) to disrupt the phase-locking necessary for resonant interactions, so that energy transfers and cross-bispectral estimates (hereinafter cross-bispectra) should be zero.

1) Frequency cross-bispectra

Frequency cross-bispectra are constructed using two complex WKB-scaled quantities $C\tilde{v}'C_y^*$ and $C\tilde{w}'C_z^*$ [see eq. (B9) for definitions] so that the real part of their sum is the contribution of the aforementioned four dominant triplets. Frequency cross-bispectra are computed at each grid point by Fourier-transforming 5-T_{ip} long time series of each property in $C\tilde{v}'C_y^*$ and $C\tilde{w}'C_z^*$ with a 20%

Tukey window to apply (B3). Tukey-windowing is chosen because wave-wave energy transfers are local and ephemeral. Final cross-bispectra are obtained by averaging the cross-bispectrum computed at every grid point enclosed by the $0.96f$ contour, that is, within the anticyclonic trapping region, and have about 3-5 degrees of freedom (cross-bispectra separated by half a vertical wavelength are regarded as independent, see Fig. 2).

The resulting cross-bispectra $B(\pm\omega_1, \pm\omega_2, \omega_1+\omega_2)$ for the two complex triplets are represented in two-dimensional frequency space as a function of ω_1 and ω_2 (Fig. 8). The daughter-wave frequency $\omega_3 = \omega_1 + \omega_2$. Frequency ω_1 corresponds to the first property in the triple product C, frequency ω_2 to the second property $\tilde{v}'$ or $\tilde{w}'$, and ω_3 to the third property involved in the wave triplet C_y^* or C_z^*. When three waves interact resonantly, non-zero cross-bispectra are obtained. Cross-bispectra satisfying $\omega_3 = -\omega_1 - \omega_2$ are negligible so not shown.

Energetic transfers involve subinertial near-inertial waves that are trapped on the anticyclonic side of the front (Fig. 8). Negative (positive) cross-bispectral values correspond to ω_1 and ω_2 transferring energy to (from) a third wave with $\omega_3 = \omega_1 + \omega_2$. Here, we focus on negative transfers from trapped subinertial waves to a superinertial wave with $\omega_3 > f$ that can escape trapping. The strongest transfers are centered at $\omega_1 = \omega_2 = 0.8f$ in $C\tilde{v}'C_y^*$ and $C\tilde{w}'C_z^*$ (Figs. 8a, b) cross-bispectra. However, these are likely components of the same triplet since they cancel out so that their physically relevant net contribution vanishes (Fig. 8c). Relevant net transfers involve either interaction between (i) $\omega_2 = 0.8f$ and $\omega_1 = f$ such that $\omega_3 = 1.8f$, or (ii) $\omega_1 = 0.8f$ and $\omega_2 = 0.6f$ such that $\omega_3 = 1.4f$ (Fig. 8c), consistent with frequencies of beams radiating out of the front in Fig. 4.

Confidence in these cross-bispectra is provided by their sum over spectral space. These agree with energy transfer rates from WKB-scaled wave triplets in the WWI term of the wave energy budget [see eqs. (B15) and (B18)]. That is, the averaged wave triplet $-\overline{\tilde{u}'\tilde{v}'\tilde{u}'_y - \tilde{v}'\tilde{v}'\tilde{v}'_y}^{xyzt} = 7.6\times10^{-11}\,\mathrm{m^2\,s^{-3}}$ over $5\,\mathrm{T_{ip}}$ and the same anticyclonic region is in agreement with $-\sum_r\sum_j \Re\{B_{C\tilde{v}'C_y^*}(\omega_r, \omega_j, \omega_r+\omega_j)\} = (7.7\pm2.7)\times10^{-11}\,\mathrm{m^2\,s^{-3}}$. Likewise, the averaged $-\overline{\tilde{u}'\tilde{w}'\tilde{u}'_z + \tilde{v}'\tilde{w}'\tilde{u}'_z}^{xyzt} = -1.07\times10^{-9}\,\mathrm{m^2\,s^{-3}}$ is comparable to $-\sum_r\sum_j \Re\{B_{C\tilde{w}'C_z^*}(\omega_r, \omega_j, \omega_r+\omega_j)\} = (-0.84\pm0.02)\times10^{-9}\,\mathrm{m^2\,s^{-3}}$. These estimates are consistent with triplets that involve vertical shear contributing most to the wave energy transfer (Fig. B1) and represent a net sink in the trapped wave energy budget (Fig. 5).

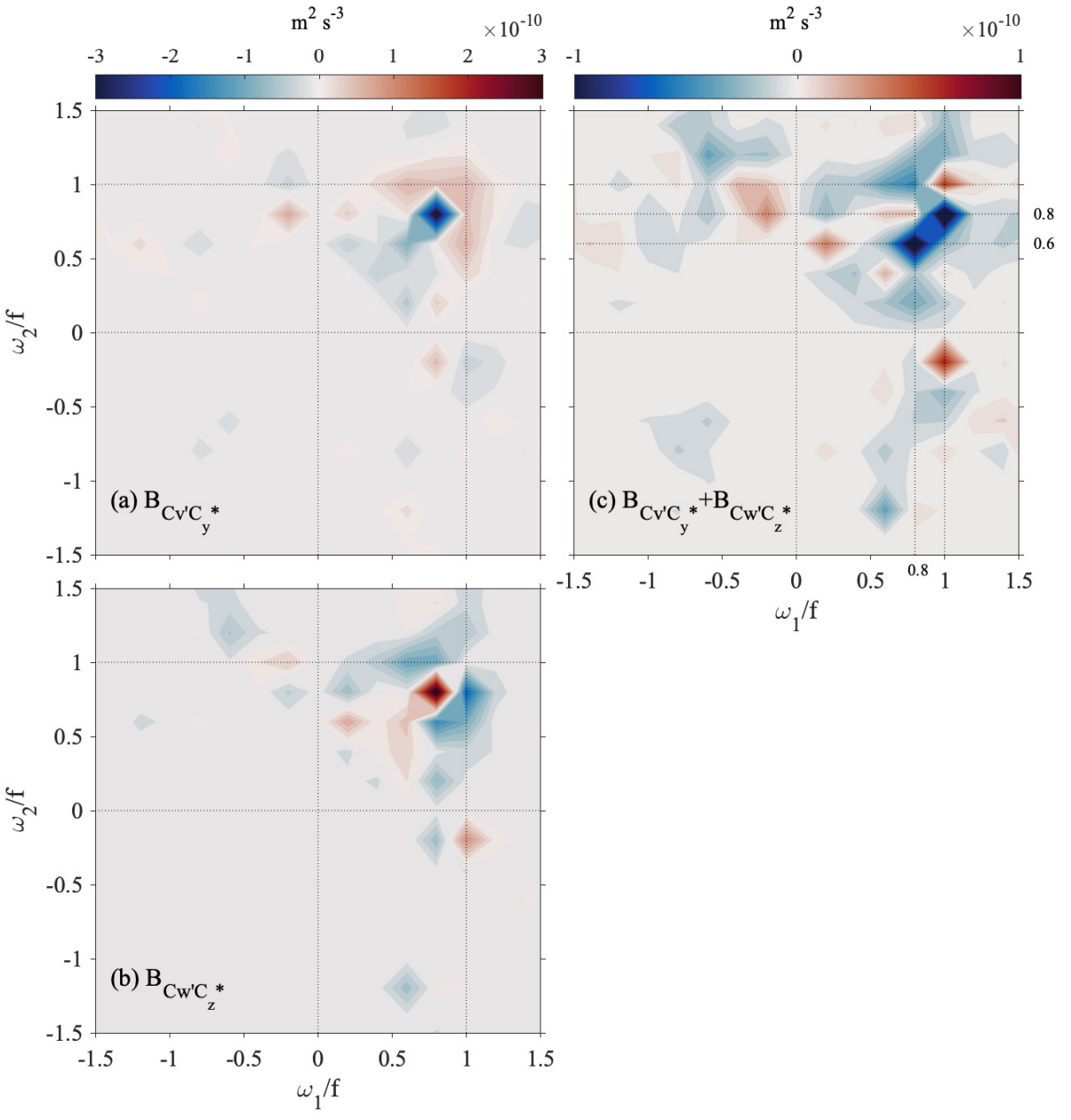

FIG. 8. Wave frequency cross-bispectra $B(\omega_1, \omega_2, \omega_1 + \omega_2)$ averaged within the anticyclonic region (grey contour in Fig. 6a) of (a) $C\tilde{v}'C_y^*$, related to triplet $\tilde{u}'\tilde{v}'\tilde{u}_y' + \tilde{v}'\tilde{v}'\tilde{v}_y'$, (b) $C\tilde{w}'C_z^*$, related to $\tilde{u}'\tilde{w}'\tilde{u}_z' + \tilde{v}'\tilde{w}'\tilde{v}_z'$, and (c) the physically relevant sum $C\tilde{v}'C_y^* + C\tilde{w}'C_z^*$ (note the magnitude change in color scale). Frequency resolution is $0.2f$ and relevant frequencies are denoted with dotted lines. Negative (blue) values indicate energy transfers from two trapped subinertial parent frequencies to a third daughter frequency. Sign convention for frequency is taken to be positive for clockwise rotation and negative for counterclockwise.

2) Vertical wavenumber cross-bispectra

Vertical wavenumber cross-bispectra are computed for complex quantities $C\tilde{v}'C_y^*$ and $C\tilde{w}'C_z^*$ as in frequency cross-bispectra. Vertical profiles of C, $\tilde{v}'$, $\tilde{w}'$, C_y, and C_z are interpolated onto a regularly spaced WKB-scaled depth axis defined by (B4), then Fourier-transformed to compute cross-bispectra at each time. The Fourier window length is 523 sm (WKB stretched meters). This window is tapered with a 40% Tukey window, suppressing inertial motions in the upper mixing layer. Final cross-bispectra are obtained by averaging cross-bispectrum computed across the anticyclonic frontal side (from $y = 54 - 74$ km) and over $5\,\mathrm{T_{ip}}$. They have about 5 degrees of freedom. As before, cross-bispectra $B(m_1, m_2, m_1 + m_2)$ are represented in two-dimensional wavenumber space (Fig. 9), where m_1 corresponds to C, m_2 to $\tilde{v}'$ or $\tilde{w}'$ and $m_3 = m_1 + m_2$ to C_y or C_z. Cross-bispectra $B(m_1, m_2, -m_1 - m_2)$ are negligible so not shown.

Strong negative energy transfers in $C\tilde{v}'C_y^*$ are centered at $m_1 = m_2 = 1.9$ cpkm (Fig. 9a). However, these are nearly balanced by positive transfers in $C\tilde{w}'C_z^*$ (Fig. 9b) so that, as before, meaningful transfers only emerge after summing these two cross-bispectral components. The resulting net transfers are mostly negative and at positive wavenumbers (Fig. 9c). The most energetic transfer involves $m_1 = 3.8$ cpkm and $m_2 = m_1/2$, transferring energy to $m_3 = m_1 + m_2 = 3m_2$.

Finally, these cross-bispectra are consistent with energy transfer rates in physical space (WWI in the energy budget) via relationships (B19) and (B20). The averaged WKB-scaled wave triplets $\overline{\tilde{u}'\tilde{v}'\,\tilde{u}'_y + \tilde{v}'\tilde{v}'\,\tilde{v}'_y}^{xyzt} = 4.6\times10^{-11}\mathrm{m^2\,s^{-3}}$ over the anticyclonic region and over $5\,\mathrm{T_{ip}}$ gives is in agreement with $-\sum_r\sum_j \Re\{B_{C\tilde{v}'C_y}(m_r, m_j, m_r + m_j)\} = (4.9 \pm 1.0)\times10^{-11}\,\mathrm{m^2\,s^{-3}}$. Likewise, the averaged $\overline{\tilde{u}'\tilde{w}'\,\tilde{u}'_z + \tilde{v}'\tilde{w}'\,\tilde{v}'_z}^{xyzt} = -6.6\times10^{-11}\mathrm{m^2\,s^{-3}}$ is consistent with $-\sum_r\sum_j \Re\{B_{C\tilde{w}'C_z}(m_r, m_j, m_r + m_j)\} = (-6.9 \pm 0.8)\times10^{-11}\,\mathrm{m^2\,s^{-3}}$. These numbers differ from those for the frequency cross-bispectra because they are integrated over a different domain.

3) Frequency-wavenumber spectra

Cross-bispectral analyses separately identified coherent frequencies and vertical wavenumbers. Here, both spectral spaces are related through the rotary frequency-wavenumber spectrum. This spectrum is computed by 2D Fourier-transforming time series of vertical profiles of complex WKB-scaled horizontal velocity C and averaging over the anticyclonic side of the front. Time and

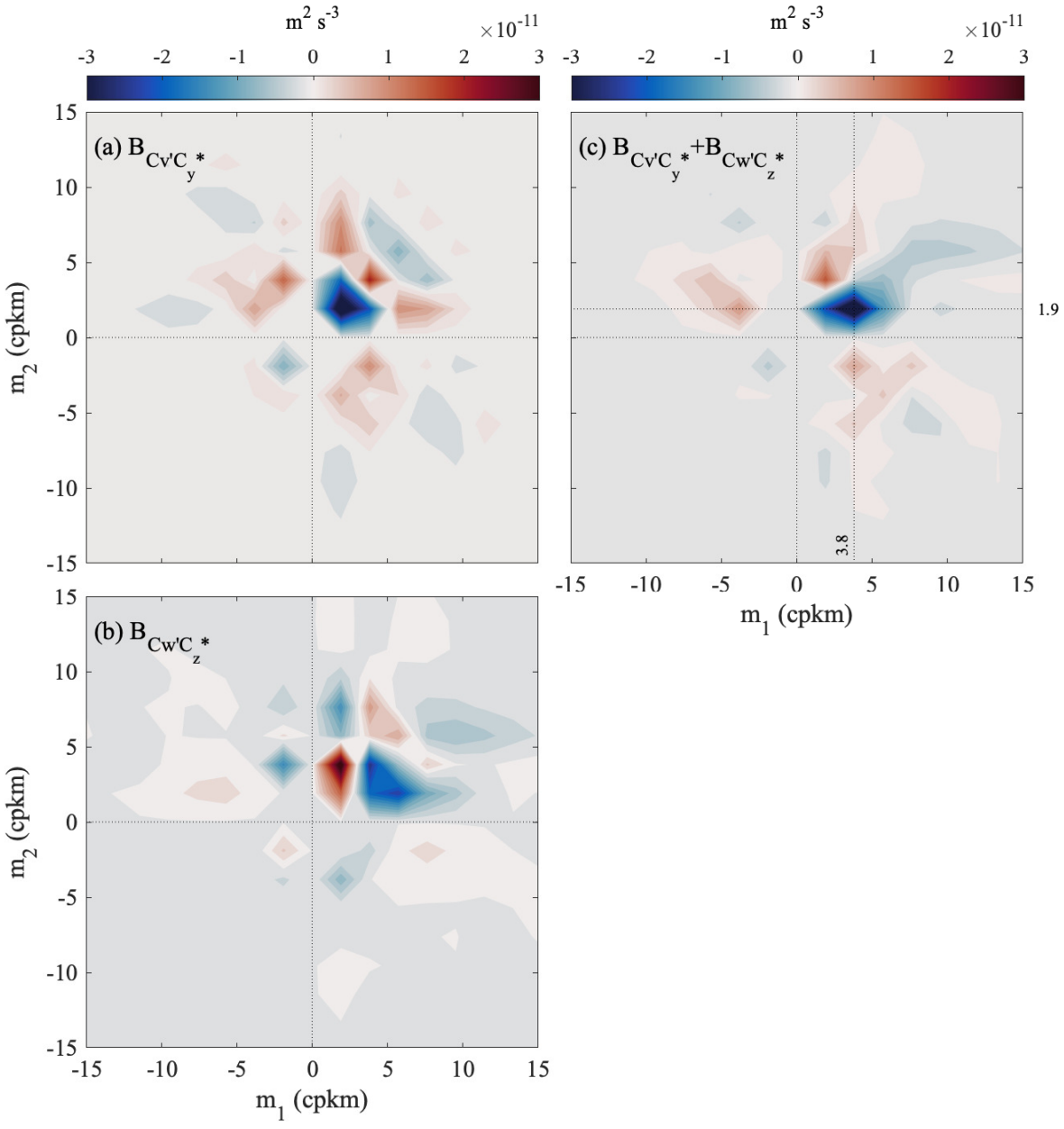

FIG. 9. Vertical wavenumber cross-bispectra $B(m_1, m_2, m_1+m_2)$ averaged in time and over the anticyclonic side of the front for (a) $C\tilde{v}'C_y^*$, related to the WKB-scaled wave triplet $\tilde{u}'\tilde{v}'\tilde{u}'_y + \tilde{v}'\tilde{v}'\tilde{v}'_y$, (b) $C\tilde{w}'C_z^*$, related to the WKB-scaled wave triplet $\tilde{u}'\tilde{w}'\tilde{u}'_z + \tilde{v}'\tilde{w}'\tilde{v}'_z$, and (c) $C\tilde{v}'\,C_y^*$+$C\tilde{w}'\,C_z^*$. Strong net resonant interactions are centered at $m_1 = 3.8$ cpkm and $m_2 = m_1/2$ (dashed lines), transferring energy to a third wave with $m_3 = m_1 + m_2$. Vertical wavenumber resolution is 1.9 cpkm.

depth extensions and tapering windows are the same as used to compute frequency and vertical wavenumber cross-bispectra.

Combining the information from frequency and vertical wavenumber cross-bispectra, two pairs of parent waves are identified (Figs. 8c, 9c):

- $(\omega_1, m_1, \omega_2, m_2) = (f, 3.8\,\text{cpkm}, 0.8f, 1.9\,\text{cpkm})$.
- $(\omega_1, m_1, \omega_2, m_2) = (0.8f, 3.8\,\text{cpkm}, 0.6f, 1.9\,\text{cpkm})$.

The ω-m space of these parent waves corresponds to where large power spectral densities are observed (white square in Fig. 10) because they correspond to trapped subinertial waves that experience amplification through wave-front interaction. Daughter waves (black square in Fig. 10) will have:

- $\omega_3 = \omega_1 + \omega_2 = 1.8f$ and $1.4f$.
- $m_3 = m_1 + m_2 = 5.7$ cpkm.

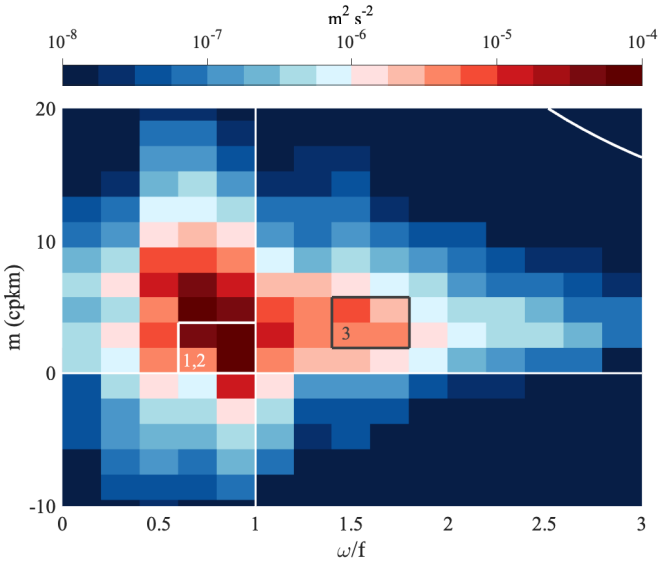

FIG. 10. Average rotary frequency-vertical wavenumber power spectra of WKB-scaled wave horizontal velocity $\tilde{u}' + i\tilde{v}'$ over the anticyclonic side of the front. White and black numbers denote waves involved in the triad. Parent-wave frequencies $(0.6f - f)$ (white square) transfer energy to daughter-wave frequencies $\omega_3 = \omega_1 + \omega_2 = (1.4f - 1.8f)$ (black space). Frequency and vertical wavenumber resolutions are $0.2f$ and 1.9 cpkm, respectively. The minimum wave aspect ratio resolved numerically (see Appendix A) is denoted with a white diagonal line at the top right corner with the spectral space below and to the left well-resolved.

This daughter-wave frequency range is above $\max(f_e) = 1.4f$, a conservative upper bound of the frequency range imposed by wave-front interactions on the cyclonic side of the front so potentially represent free waves. As parent and daughter waves all have positive vertical wavenumbers, their phases propagate upward and energy downward in agreement with Figs. 4, 6a.

c. Across-front wavenumbers

Having identified coherent frequencies ω and vertical wavenumbers m for what we will assume are the parent waves of two resonant triads from the cross-bispectra (Figs. 8, 9), the corresponding parent-wave cross-front wavenumbers ℓ can be determined from the front dispersion relation

$$\ell_\pm = \frac{\bar{b}_y m}{N_0^2}\left(1 \pm \sqrt{1 + \frac{N_0^2(\omega^2 - f_e^2)}{\bar{b}_y^2}}\right) \tag{8}$$

(Mooers 1975a; Kunze 1985; Whitt and Thomas 2013). Taking $\bar{\zeta} = -0.68f$, $\bar{b}_y = -9.6\times10^{-8}$ s^{-2} ($Fr = 0.37$), and $N_0^2 = 9.6\times10^{-6}$ rad^2 s^{-2}, for the first parent-wave pair (Fig. 11a, black and blue squares):

- $(\omega_1, m_1) = (f, 3.8\,\text{cpkm})$, $\ell_{1\pm} = -0.13, 0.05$ cpkm ($\lambda_y \sim 8, 18$ km).
- $(\omega_2, m_2) = (0.8f, 1.9\,\text{cpkm})$, $\ell_{2\pm} = -0.054, 0.016$ cpkm ($\lambda_y \sim 18, 64$ km).

And for the other parent-wave pair (Fig. 12a, black and blue squares):

- $(\omega_1, m_1) = (0.8f, 3.8\,\text{cpkm})$, $\ell_{1\pm} = -0.11, -0.03$ cpkm ($\lambda_y \sim 9, 32$ km).
- $(\omega_2, m_2) = (0.6f, 1.9\,\text{cpkm})$, $\ell_{2\pm} = -0.04, 0.0026$ cpkm ($\lambda_y \sim 25, 385$ km).

d. Daughter waves

It is assumed that the daughter frequency $\omega_3 = \omega_1 + \omega_2$ so as to exceed f (Figs. 8c,11a,12a), and the vertical wavenumber $m_3 = m_1 + m_2$ (Figs. 9, 11a, 12a). Considering three plane waves, these relations restrict the potential daughter-wave cross-front wavenumbers to $\ell_3 = \ell_{1\pm} + \ell_{2\pm}$ with the additional requirement that, to ensure resonance, the daughter-wave $\omega(\ell_3, m_3) = \omega_1 + \omega_2$, that is, either the front or quiescent ocean dispersion relation must yield the same frequency as the resonant condition; in practice, we require that the two agree to within 15%, within the frequency resolution

of the bispectra (Fig. 8). Of the four possible ℓ_3 inferred for the first parent pair, all conditions for resonance are satisfied for:

- $\ell_3 = -0.18$ cpkm ($\lambda_y \sim 5$ km) and $\omega_3 = 1.56f$ (Fig. 11, solid red square).

And for:

- $\ell_3 = -0.15$ cpkm ($\lambda_y \sim 7$ km) and $\omega_3 = 1.39f$ (Fig. 12, solid red square),
- $\ell_3 = -0.1$ cpkm ($\lambda_y \sim 10$ km) and $\omega_3 = 1.21f$ (Fig. 12, void red square).

All of them are from the quiescent dispersion relation with no solutions found for the front dispersion relation in any of the cases. This example illustrates that wave triads can explain superinertial wave beams propagating south and downwards in Fig. 4b. While solutions for superinertial wave beams propagating north and downwards have not been found, secondary nonlinear wave-wave interactions may account for them.

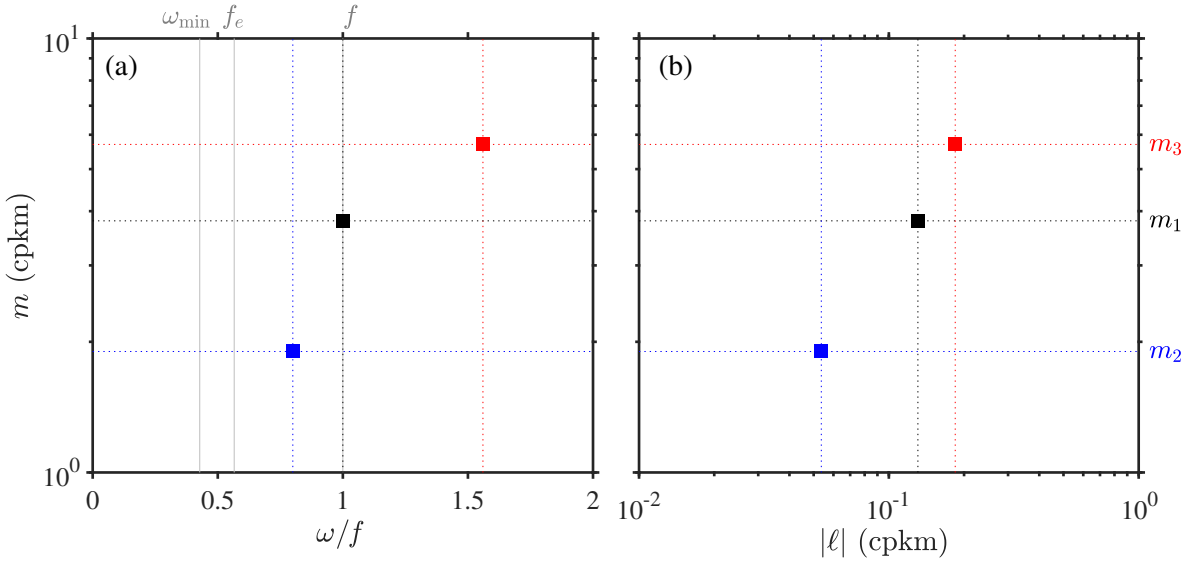

FIG. 11. For moderate $Fr = 0.37$ and strong $Ro = -0.68$, $\omega_1 = f$ and $\omega_2 = 0.8f$ – (a) Vertical wavenumber magnitudes m and frequencies ω/f for parent-wave 1 (black), parent-wave 2 (blue) and free daughter-wave 3 (red) with $\omega_3 = 1.56f$ and $m_3 = m_1 + m_2$. (b) Vertical wavenumber m as a function of across-front wavenumber magnitude $|\ell|$ for the parent-wave pair solution from the front dispersion relation with $\ell_{1+} = -0.13$ cpkm ($\lambda_y \sim 8$ km) for wave 1, with $\ell_{2+} = -0.054$ cpkm ($\lambda_y \sim 18$ km) for wave 2 and with free-wave across-front wavenumber $\ell_3 = \ell_{1+} + \ell_{2+} = -0.18$ cpkm ($\lambda_y \sim 5$ km) for wave 3. Only one free wave is allowed, for the quiescent dispersion relation.

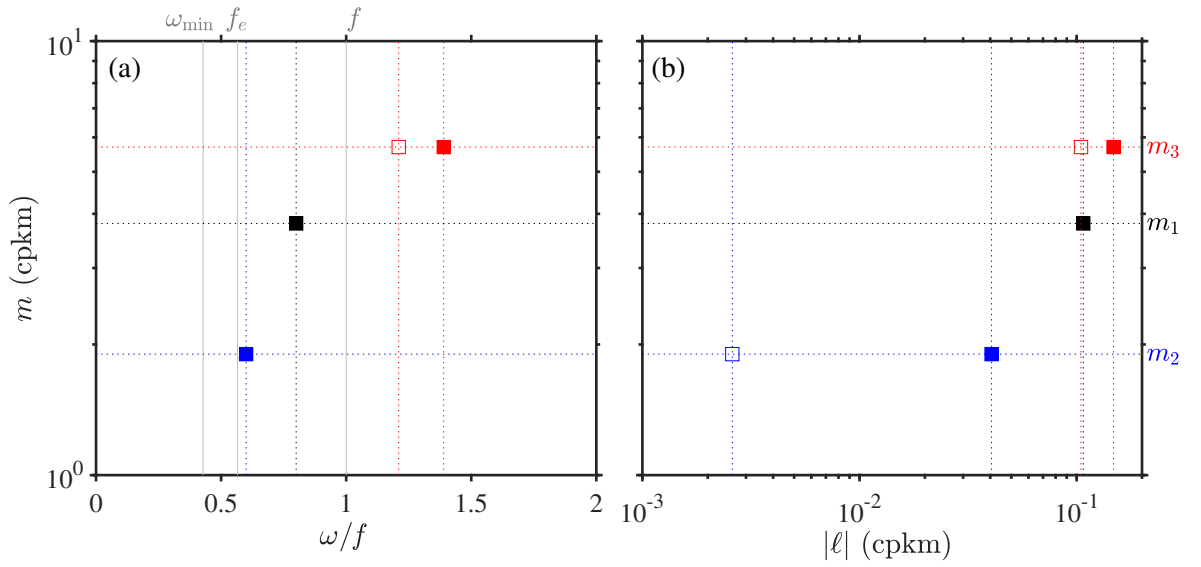

FIG. 12. As in Fig. 11 but for triads with $\omega_1 = 0.8f$ and $\omega_2 = 0.6f$ – In (a) daughter-waves 3 (red) have frequencies with $\omega_3 = 1.39, 1.21f$. In (b) across-front wavenumbers for parent-wave 1 (black) is $\ell_{1+} = -0.11$ cpkm ($\lambda_y \sim 9$ km, solid square), for parent-wave 2 (blue) are $\ell_{2+} = 0.04$ cpkm ($\lambda_y \sim 25$ km, solid square) and $\ell_{2-} = 0.0026$ cpkm ($\lambda_y \sim 385$ km, void square) and for free waves (red) are $\ell_3 = \ell_{1+} + \ell_{2+} = -0.15$ cpkm ($\lambda_y \sim 7$ km) and $\ell_3 = \ell_{1+} + \ell_{2-} = -0.1$ cpkm ($\lambda_y \sim 10$ km). Only two free waves are allowed, both for the quiescent ocean dispersion relation.

The wave-wave interactions discussed here involve scale-separation of about a factor of two in frequency and vertical wavenumber space and roughly a factor of three in horizontal wavenumber. These interactions do not resemble any of the three classic wave triads described by McComas and Bretherton (1977) using extreme scale-separated limits. Instead, they fall within spectrally local interactions recently identified to be far from negligible within the internal wave field using scale-invariant solutions of the internal-wave kinetic energy equation (Dematteis and Lvov 2021; Dematteis et al. 2022) as well as in numerical solutions that account for rotation (Wu and Pan 2023). These spectrally local interactions are important because they transfer energy toward higher vertical shears.

e. Froude and Rossby number space

Also of interest is the balanced Ro, Fr parameter space for which free-wave escape is possible through wave-wave interactions. The modeled jet is based on the Gulf Stream with front vorticity

$Ro = -0.85$ and front gradient Froude numbers $Fr = 0.8$ which are much stronger than typically found in mesoscale fronts and eddies. Resonant solutions were sought as a function of these two nondimensional front parameters (Fig. 13). High Froude and strong vorticity Rossby numbers are excluded because then the front potential vorticity $q = f^2 N_0^2 (1 + Ro - Fr^2) < 0$ and the minimum frequency $\omega^2_{\rm min} < 0$ (gray shading), both indicating growing instabilities rather than oscillations for trapped motions. Assuming $\omega_1 = \omega_2$, free-wave generation is confined to a narrow band in Froude number-Rossby number space for the quiescent dispersion relation only. Free waves can arise for $0 < 1 + Ro - Fr^2 < 0.36$ so that either Ro or Fr have to be moderately high. To generalize, either vorticity (Ro) or baroclinicity (Fr) have to be moderately strong for free-wave escape from vorticity and baroclinicity trapping of near-inertial waves. There can be no free-wave escape for low Fr and low Ro ($1 + Ro - Fr^2 > 0.36$, Fig. 13) which makes free-wave escape less likely for typical mesoscale eddies.

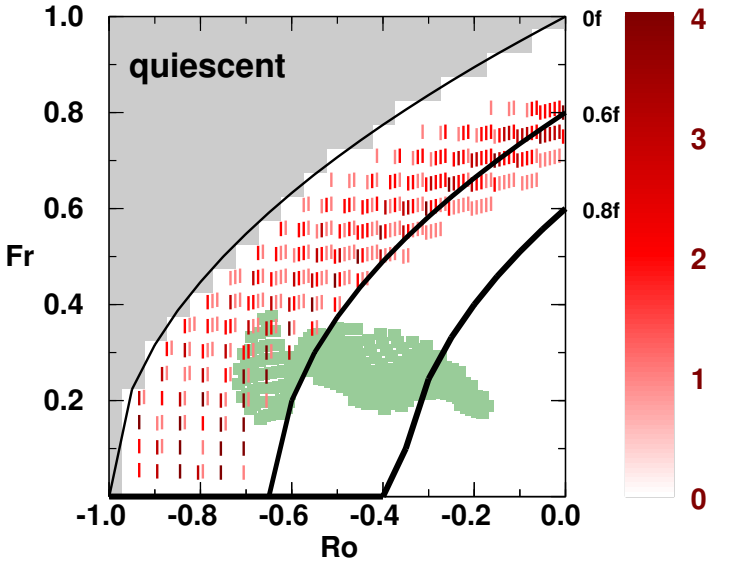

FIG. 13. Free-wave escape as a function of front gradient Froude number Fr and vorticity Rossby number Ro assuming the free waves satisfy the quiescent dispersion relation. Gray shading blocks out the domain where mean-flow potential vorticity $\bar{q} < 0$ and $\omega^2_{\rm min} < 0$ so that instabilities are expected rather than trapped near-inertial waves. Red hashmarks denote the number of free waves ($\omega_3 = \omega_1 + \omega_2$) that are allowed (color bar) for $\omega_1 = \omega_2$ at 5 frequencies between $\omega_{\rm min}$ and f. Black curves denote $\omega_{\rm min} = f\sqrt{1 + Ro - Fr^2} = 0, 0.6f$ and $0.8f$, and the green shading describes the Fr-Ro relationship within the anticyclonic frontal side where wave-wave interactions represent an energy sink (see Fig. 6b).

Several limitations can explain why the region where wave-wave interactions represent an energy sink within the anticyclonic side of the front (Fig. 6b) extends above the $1 + Ro - Fr^2 = 0.36$ parameter space (green shading in Fig. 13). First, the Ro-Fr parameter space exploration in this section uses identical frequencies and vertical wavenumbers for the two parent waves. Second, the numerical simulation considers only a single initial wind event and it has not reached a stationary steady over the first 5 T_{ip} considered for analyses. Third, inferred parent-wave frequency uncertainties $\pm 0.2f$ (Fig. 8) and vertical wavenumber ones ± 1.9 cpkm (Fig. 9) encompass ranges not considered in the calculation of parent-wave across-front wavenumbers and daughter-wave properties (Figs. 11 and 12).

6. Concluding remarks

We have explored novel wave-triad interactions among energetic near-inertial waves that allow wind-generated wave energy trapped within anticyclonic vorticity to radiate into the quiescent surrounding ocean. The interactions transfer energy from two trapped near-inertial parent waves to a superinertial daughter wave of higher vertical wavenumber that is free to escape. These three waves are separated in frequency and wavenumber space by a factor of two to three, falling within spectrally local interactions that have recently found to be non-negligible in the forward energy cascade towards dissipative scales (Dematteis and Lvov 2021; Dematteis et al. 2022; Wu and Pan 2023). Wave-triad generation of free waves that can escape anticyclonic trapping only appear to be possible for fronts with either strong baroclinicity (Fr) or strong vorticity (Ro) such that $0 < 1 + Ro - Fr^2 < 0.36$ (Fig. 13). This is more common in submesoscale surface fronts and filaments than mesoscale eddies, though also found in western boundary currents as modeled here.

In this idealized simulation, wave triads occur in a wind-forced front but the results can be extended to strong three-dimensional baroclinic anticyclones that trap subinertial waves in their interior since wave confinement likely facilitates wave phase-coupling. Generally, dissipation competes with escape of trapped waves as a wave energy sink within the eddy. Here, the dissipative sink is about twice that from wave-wave interactions. While turbulent dissipation is likely underestimated by using a constant viscosity of $O(10^{-4})$ m^2/s, one order of magnitude smaller than that observed in anticyclones (Lueck and Osborn 1986; Kunze and Toole 1997), we have also only considered a one-time wind event. The sink associated with wave-triad interactions may be

further enhanced with more sustained wind forcing such as mid-latitude or tropical storms passing over strong oceanic fronts than an isolated wind event. Including an ambient internal-wave field will also likely facilitate more nonlinear interactions.

For ultimate evaluation of whether the wave triads reported here could make an impact on the regional frequency spectra at depth, by injecting wind-generated wave energy within a continuum frequency band from f to $2f$, a shear-driven dissipation scheme or nested simulations of increased spatial resolution (e.g. Winters et al. 2024) would be needed. These simulations should explore a broader balanced Rossby-Froude number parameter space than considered here.

Acknowledgments. This work greatly benefited from conversations with Pascale Lelong, David Straub and Jonathan Lilly. Funding provided by the Office of Naval Research, LatMix DRI under Grant N000141210101 (MC, AM) and the US National Science Foundation under grants OCE-1850761 (MC), OCE-2318952 (MC), OCE-2045270 (EK), OCE-2068285 (EK), OCE-1634644 (KP) is gratefully acknowledged. Bispectral code is based on Swami et al. (2014).

Data availability statement. PSOM is an open source model. The numerical code specific to the simulation documented in this manuscript is available at `https://github.com/PSOM/V0.63/blob/master/code/waves`. Model output will be made publicly available via Zenodo before manuscript publication.

APPENDIX A

Sensitivity to background diffusivity and non-hydrostatic effects

We discuss the robustness of the results by considering numerical resolution and background diffusivity. Existing wave triads are obscured in numerical simulations when energy is transferred to unresolved scales, that is, to scales close to grid resolution so that diffusive processes remove energy faster than nonlinear energy transfer rates (Winters et al. 2004). As a result, energy either accumulates due to insufficient grid resolution or dissipates at the maximum resolvable wavenumber. For this reason, we analyze both the appropriateness of the numerical resolution used, and sensitivity of the wave-wave energy transfer rates to different diffusivities. Additionally, we quantify wave-wave interactions under the hydrostatic approximation.

First, we check that nonlinear wave-triad transfers are resolved in our numerical scenario, where the maximum horizontal wavenumber resolved is $\ell^{\max} = 1/800\,\mathrm{cpm}$. Assuming a linear wave dispersion relation in 2-D and constant buoyancy frequency for simplicity, the wave dispersion curve corresponding to $\ell^{\max}$ is $\omega^2 = f^2 + (N_0(\ell^{\max}/m)^2$. Overlying this curve with the $(\omega - m)$-spectrum (thick solid line in Fig. 10) shows that the wave triad is resolved.

Second, we quantify the sensitivity of the wave-triad strength to different diffusivities in terms of the cross-front integrated WWI term corresponding to wave-wave net energy transfers in (5). When the horizontal diffusivity is halved, wave-wave energy transfers are not significantly altered compared to the case previously analyzed (Fig. A1a). In contrast, when the vertical diffusivity is decreased by one order of magnitude, the wave-wave interactions are strengthened. Pressure-work increases using a smaller vertical diffusivity (Fig. A1b), because there is less energy dissipation as waves propagates downward from the surface, meaning that the source of energy for waves to interact resonantly is enhanced compared to the previously analyzed case.

Finally, running the hydrostatic version of PSOM (Mahadevan 2006) using the same numerical configuration does not modify the strength of wave triads, nor the amount of energy that propagates downward (green line in Figs. A1a,b). The hydrostatic approximation is valid when ω is much smaller than N so that wave motion is largely horizontal. In our case, the time and spatial average of N over the five inertial periods analyzed on the anticyclonic side of the front, where waves interact resonantly, is $\bar{N} = 6.9 \times 10^{-3}\,\mathrm{s}^{-1}$. Considering that the waves involved in the wave triad

603 are near-inertial, $\bar{N}/\omega \simeq \bar{N}/f$ is about 82 for a midlatitude of $35°N$. Therefore $\omega \ll \bar{N}$, and the
604 hydrostatic approximation is valid.

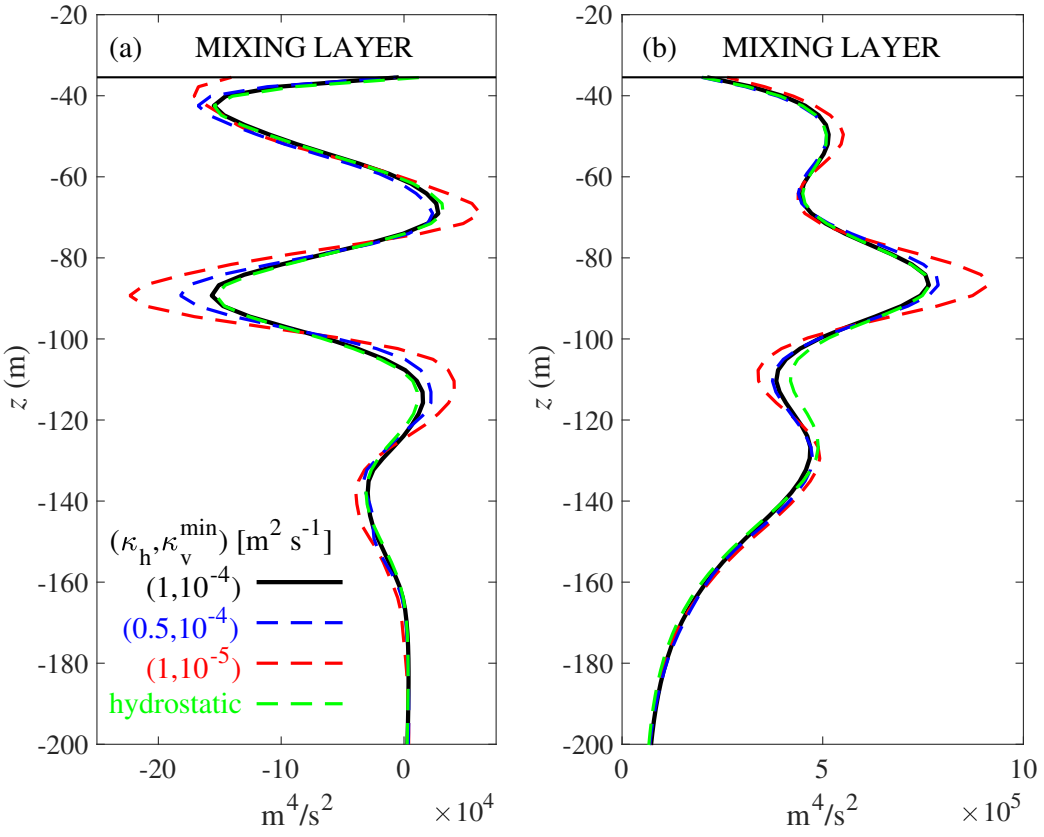

605 FIG. A1. As in Fig. 5 but for terms (a) WWI and (b) WPW considering different scenarios. The case discussed
606 so far (solid black line) is compared to three cases in which the horizontal diffusivity κ_h is halved (dashed blue
607 line), the minimum vertical diffusivity $\kappa_v^{\min}$ is decreased by one order of magnitude (dashed red line), and the
608 hydrostatic approximation is made (dashed green line). Note the different range x-axes in (a) and (b).

609 APPENDIX B

610 **Constructing cross-bispectra**

611 The cross-bispectrum is defined as the Fourier transform of the bicovariance among two inde-
612 pendent processes of wave frequencies ω_1, ω_2 and wavenumber vectors $\mathbf{k}_1$, $\mathbf{k}_2$, with a third process

of ω_3 and $\mathbf{k}_3$ that satisfy

$$\omega_1 + \omega_2 = \omega_3, \tag{B1}$$

$$\mathbf{k}_1 + \mathbf{k}_2 = \mathbf{k}_3 \tag{B2}$$

(McComas and Bretherton 1977). It is expressed as a function of two wave frequencies and wavenumbers

$$B(\omega_1, \mathbf{k}_1, \omega_2, \mathbf{k}_2) \equiv E[\hat{\chi}(\omega_1, \mathbf{k}_1)\hat{\chi}(\omega_2, \mathbf{k}_2)\hat{\chi}^*(\omega_1 + \omega_2, \mathbf{k}_1 + \mathbf{k}_2)], \tag{B3}$$

where χ is any given real process with zero mean and complex Fourier coefficient $\hat{\chi}$. Here, $(\cdot)^*$ denotes the complex conjugate, and $E[\cdot]$ is the estimated value over many realizations. Choosing the three processes as three waves involved in triplets of WWI (5), the cross-bispectrum can be understood as a decomposition in spectral space of energy transfers among three waves. Its absolute value gives the magnitude of energy transfers, while its sign the direction of these transfers.

To construct cross-bispectra, wave properties are first Wentzel-Kramers-Brillouin (WKB) normalized to remove variability in vertical wavenumbers and variables due solely to variable buoyancy frequency N. Following Gill (1982), the WKB-stretched vertical domain is defined by normalizing depth with a constant buoyancy frequency N_0 as

$$\tilde{z} = \frac{1}{N_0}\int_0^z N(z^*)\mathrm{d}z^*, \tag{B4}$$

and wave properties as

$$(\tilde{\mathbf{u}}', \tilde{\mathbf{u}}'_y) = \left(\mathbf{u}'_h, \frac{\partial \mathbf{u}'_h}{\partial y}\right)\left(\frac{N(z)}{N_0}\right)^{-1/2}, \tag{B5}$$

$$\tilde{w}' = w'\left(\frac{N(z)}{N_0}\right)^{1/2}, \tag{B6}$$

$$\tilde{\mathbf{u}}'_z = \frac{\partial \mathbf{u}'_h}{\partial z}\left(\frac{N(z)}{N_0}\right)^{-3/2}, \tag{B7}$$

where the WKB-scaled horizontal velocity vector is $\tilde{\mathbf{u}}' = (\tilde{u}', \tilde{v}')$, its lateral shear $\tilde{\mathbf{u}}'_y = (\tilde{u}'_y, \tilde{v}'_y)$, and its vertical shear $\tilde{\mathbf{u}}'_z = (\tilde{u}'_z, \tilde{v}'_z)$ This normalization is valid since non-hydrostatic effects are negligible Appendix A).

Wave frequency and vertical wavenumber cross-bispectra are constructed and related to wave-wave energy transfer rates as in Sun and Pinkel (2012, 2013). The WWI term consists of nine triplets in this configuration. However, only four triplets by inspection have a significant contribution when integrated across the front (Fig. B1), that is, $\mathbf{u}' \cdot \mathbf{u}' \cdot \nabla \mathbf{u}' \cong u'v'u'_y + v'v'v'_y + u'w'u'_z + v'w'v'_z$. To discriminate between positive and negative wave frequencies and wavenumbers, these triplets are WKB-scaled and expressed in complex form

$$\tilde{\mathbf{u}}'_h \cdot \tilde{v}' \partial \tilde{\mathbf{u}}'_h / \partial y = \Re\{C\, \tilde{v}' C_y^*\} \quad \text{and} \quad \tilde{\mathbf{u}}'_h \cdot \tilde{w}' \partial \tilde{\mathbf{u}}'_h / \partial z = \Re\{C\, \tilde{w}' C_z^*\}, \tag{B8}$$

where

$$C \equiv \tilde{u}' + i\tilde{v}', \quad C_y \equiv \tilde{u}'_y + i\tilde{v}'_y, \quad \text{and} \quad C_z \equiv \tilde{u}'_z + i\tilde{v}'_z. \tag{B9}$$

Next, we derive the time-averaged triple-product $C\, \tilde{v}' C_y^*$ in frequency space by considering the Fourier time series of the properties involved. For complex quantities C and C_y, these are

$$C(t) = \sum_r \hat{\mathcal{U}}(-\omega_r) e^{-i\omega_r t} + \hat{\mathcal{U}}(+\omega_r) e^{i\omega_r t} \quad \text{and} \quad C_y(t) = \sum_k \hat{\mathcal{Y}}(-\omega_k) e^{-i\omega_k t} + \hat{\mathcal{Y}}(+\omega_k) e^{i\omega_k t}, \tag{B10}$$

where frequency $\omega_r = 2\omega^{\max} |r/n|$ for an n-point Fourier time window with $r = -n/2, \ldots, n/2 - 1$, being the critical Nyquist frequency $\omega^{\max} = \pi/\Delta t$. The real quantity $\tilde{v}'$ is first decomposed into anticlockwise and clockwise motions (denoted with - and + subscripts) using $\tilde{\mathbf{u}}'_h$. Both components are then Fourier-transformed to get

$$\tilde{v}'(t) = \tilde{v}'_-(t) + \tilde{v}'_+(t) = \sum_j 2\hat{\mathcal{V}}_-(-\omega_j) e^{-i\omega_j t} + 2\hat{\mathcal{V}}_+(+\omega_j) e^{i\omega_j t}. \tag{B11}$$

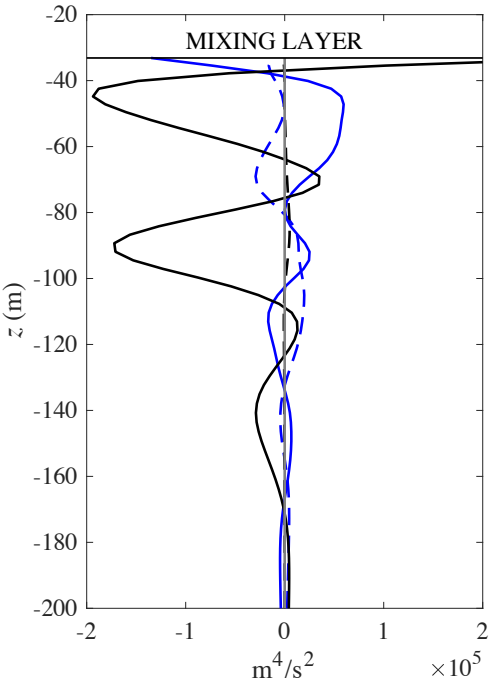

FIG. B1. Vertical profiles of four wave energy triplets, namely $u'v'u'_y$ (dashed blue line), $u'w'u'_z$ (solid blue line), $v'v'v'_y$ (dashed black line), and $v'w'v'_z$ (solid black line). These triplets account for the total of the wave/wave interaction term (WWI, red line) of the wave energy budget when integrated over $5T_{\rm ip}$ (see residual in gray between WWI and the sum of the four wave triplets selected). These four wave triplets are the ones considered when computing cross-bispectra.

Multiplying the three complex quantities, we obtain

$$\begin{aligned} C\,\tilde{v}'C_y^* &= \sum_r \left\{\hat{\mathcal{U}}(-\omega_r)e^{-i\omega_r t} + \hat{\mathcal{U}}(+\omega_r)e^{i\omega_r t}\right\} \\ &\quad \sum_j \left\{2\hat{\mathcal{V}}_-(-\omega_j)e^{-i\omega_j t} + 2\hat{\mathcal{V}}_+(+\omega_j)e^{i\omega_j t}\right\} \\ &\quad \sum_k \left\{\hat{\mathcal{Y}}^*(-\omega_k)e^{i\omega_k t} + \hat{\mathcal{Y}}^*(+\omega_k)e^{-i\omega_k t}\right\} \\ &= \sum_r \sum_j \sum_k \hat{\mathcal{U}}(-\omega_r)2\hat{\mathcal{V}}_-(-\omega_j)\hat{\mathcal{Y}}^*(-\omega_k)e^{i(-\omega_r-\omega_j+\omega_k)t} + \text{c.c.}, \end{aligned} \tag{B12}$$

where c.c. refers to complex conjugates. Time-averaging over the Fourier window, all exponential terms go to zero except when resonant conditions are fulfilled (B1). As a result, time-averaged

wave energy triplets depend only on two independent frequencies

$$\overline{C\,\tilde{v}'C_y^*}^t = \sum_r \sum_j \hat{\mathcal{U}}(-\omega_r)\,\hat{\mathcal{V}}_-(-\omega_j)\hat{\mathcal{Y}}^*(-\omega_r-\omega_j) + \text{c.c.} \tag{B13}$$

Finally, this expression is related to the frequency bispectrum by considering the estimated value of many realizations in space (B3),

$$\overline{C\,\tilde{v}'C_y^*}^{xyzt} = \sum_r \sum_j B(-\omega_r, -\omega_j, -\omega_r-\omega_j) + \text{c.c.}, \tag{B14}$$

or

$$\overline{C\,\tilde{v}'C_y^*}^{xyzt} = \sum_r \sum_j \left\{B(\pm\omega_r, \pm\omega_j, -\omega_r-\omega_j) + B(\pm\omega_r, \pm\omega_j, \omega_r+\omega_j)\right\} \tag{B15}$$

to include all eight linear combinations of the three waves.

The second wave energy triplet of interest $C\,\tilde{w}'C_z^*$ is related to cross-bispectra in a similar way, but considers $\tilde{w}'$ and C_z in terms of the Fourier series

$$\begin{aligned}
\tilde{w}'(t) &= \tilde{w}'_-(t) + \tilde{w}'_+(t) \\
&= \sum_j 2\hat{\mathcal{W}}(-\omega_j)R(-\omega_j)e^{-i\omega_j t} + 2\hat{\mathcal{W}}(+\omega_j)R(+\omega_j)e^{i\omega_j t}, \qquad \text{(B16)} \\
C_z(t) &= \sum_k \hat{\mathcal{Z}}(-\omega_k)e^{-i\omega_k t} + \hat{\mathcal{Z}}(+\omega_k)e^{i\omega_k t}, \qquad \text{(B17)}
\end{aligned}$$

where $R(-\omega_j) = |\hat{\mathcal{U}}(-\omega_j)|^2/(|\hat{\mathcal{U}}|(-\omega_j)|^2 + |\hat{u}(\omega_j)|^2)$ is the ratio of anticlockwise to total horizontal velocity variance at a given frequency. Analogously, $R(\omega_j)$ is the ratio of clockwise to total velocity variance. Introducing the R ratio allows differentiation between vertical velocity associated with anticlockwise vs clockwise motions, improving the numerical agreement between energy transfers in physical space and cross-bispectra, both related through

$$\overline{C\,\tilde{w}'C_z^*}^{xyzt} = \sum_r \sum_j \left\{B(\pm\omega_r, \pm\omega_j, -\omega_r-\omega_j) + B(\pm\omega_r, \pm\omega_j, \omega_r+\omega_j)\right\}. \tag{B18}$$

Vertical wavenumber cross-bispectra is constructed analogously to frequency cross-bispectra so that energy transfers in physical and spectral space are related through

$$\overline{C\,\tilde{v}'\,C_y^*}^{xyzt} = \sum_r \sum_j \left\{ B(\pm m_r, \pm m_j, -m_r - m_j) + B(\pm m_r, \pm m_j, m_r + m_j) \right\}, \tag{B19}$$

$$\overline{C\,\tilde{w}'\,C_z^*}^{xyzt} = \sum_r \sum_j \left\{ B(\pm m_r, \pm m_j, -m_r - m_j) + B(\pm m_r, \pm m_j, m_r + m_j) \right\}. \tag{B20}$$

Finally, statistical significance of the cross-bispectra is quantified by randomly shifting the phase of one of the three processes (Naveira Garabato et al. 2022). Synthetic cross-bispectra are generated by randomizing the phase of the first property in triplets at each grid point and averaging over the anticyclonic region to obtain one estimate. 95% confidence intervals are computed from 1,000 synthetic cross-bispectral estimates. This approach is chosen because the limited number of degrees of freedom (5 in time and 2-3 in space for 2 velocity components) challenges bicoherence, the statistic commonly used to test significance of cross-bispectra. Moreover, the wave-wave interactions reported here are likely more heterogenous and nonstationary in space and time than assumed in statistical uncertainty analyses.

References

Alford, M. H., 2020: Revisiting near-inertial wind work: Slab models, relative stress, and mixed layer deepening. *Journal of Physical Oceanography*, **50 (11)**, 3141–3156, https://doi.org/10.1175/JPO-D-20-0105.1.

Alford, M. H., M. F. Cronin, and J. M. Klymak, 2012: Annual cycle and depth penetration of wind-generated near-inertial internal waves at ocean Station Papa in the Northeast Pacific. *J. Phys. Oceanogr.*, **42**, 889–909.

Asselin, O., L. N. Thomas, W. R. Young, and L. Rainville, 2020: Refraction and straining of near-inertial waves by barotropic eddies. *Journal of Physical Oceanography*, **50 (12)**, 3439 – 3454, https://doi.org/10.1175/JPO-D-20-0109.1, URL https://journals.ametsoc.org/view/journals/phoc/50/12/JPO-D-20-0109.1.xml.

Asselin, O., and W. R. Young, 2020: Penetration of wind-generated near-inertial waves into a turbulent ocean. *Journal of Physical Oceanography*, **50 (6)**, 1699 – 1716, https://doi.org/

https://doi.org/10.1175/JPO-D-19-0319.1.

Carter, G. S., and M. C. Gregg, 2006: Persistent near-diurnal internal waves observed above a site of m2 barotropic-to-baroclinic conversion. *J. Phys. Oceanogr.*, **36 (6)**, 1136–1147, https://doi.org/10.1175/JPO2884.1.

Chaigneau, A., O. Pizarro, and W. Rojas, 2008: Global climatology of near-inertial current characteristics from lagrangian observations. *Geophys, Res. Lett.*, **35 (13)**, n/a–n/a, https://doi.org/10.1029/2008GL034060, l13603.

Claret, M., and A. Viúdez, 2010: Vertical velocity in the interaction between inertia–gravity waves and submesoscale baroclinic vortical structures. *J. Geophys. Res.*, **115 (C12)**, https://doi.org/10.1029/2009JC005921.

Cuypers, Y., X. Le Vaillant, P. Bouruet-Aubertot, J. Vialard, and M. J. McPhaden, 2013: Tropical storm-induced near-inertial internal waves during the Cirene experiment: Energy fluxes and impact on vertical mixing. *J. Geophys. Res.*, **118 (1)**, 358–380, https://doi.org/10.1029/2012JC007881.

Danioux, E., P. Klein, M. W. Hecht, N. Komori, G. Roullet, and S. L. Gentil, 2011: Emergence of wind-driven near-inertial waves in the deep ocean triggered by small-scale eddy vorticity structures. *J. Phys. Oceanogr.*, **41**, 1297—1307.

Danioux, E., P. Klein, and P. Rivière, 2008: Propagation of wind energy into the deep ocean through a fully turbulent mesoscale eddy field. *J. Phys. Oceanogr.*, **38**, 2224—-2241.

Danioux, E., J. Vanneste, and O. Bühler, 2015: On the concentration of near-inertial waves in anticyclones. *Journal of Fluid Mechanics*, **773**, R2, https://doi.org/10.1017/jfm.2015.252.

D'Asaro, E. A., 1989: The decay of wind-forced mixed layer inertial oscillations due to the β effect. *J. Geophys. Res.*, **94 (C2)**, 2045–2056.

D'Asaro, E. A., 1995: Upper-ocean inertial currents forced by a strong storm. part iii: Interaction of inertial currents and mesoscale eddies. *Journal of Physical Oceanography*, **25 (11)**, 2953–2958, https://doi.org/10.1175/1520-0485(1995)025⟨2953:UOICFB⟩2.0.CO;2.

712 D'Asaro, E. A., C. C. Eriksen, M. D. Levine, C. A. Paulson, P. Niiler, , and P. V. Meurs, 1995:
713 Upper-ocean inertial currents forced by a strong storm. Part I: Data and comparisons with linear
714 theory. *J. Phys. Oceanogr.*, **25**, 2909–2936.

715 Dematteis, G., B. Arnaud Le F. Pollmann, K. Polzin, M. Alford, C. B. Whalen, and Y. V.
716 Lvov, 2024: Interacting internal waves explain global patterns of interior ocean mixing. *Nature*
717 *Communications*, **15 (7468)**, https://doi.org/10.1038/s41467-024-51503-6.

718 Dematteis, G., and Y. V. Lvov, 2021: Downscale energy fluxes in scale-invariant oceanic internal
719 wave turbulence. *Journal of Fluid Mechanics*, **915**, A129, https://doi.org/10.1017/jfm.2021.99.

720 Dematteis, G., K. Polzin, and Y. V. Lvov, 2022: On the origins of the oceanic ultraviolet catastrophe.
721 *Journal of Physical Oceanography*, **52 (4)**, 597 – 616, https://doi.org/10.1175/JPO-D-21-0121.1,
722 URL https://journals.ametsoc.org/view/journals/phoc/52/4/JPO-D-21-0121.1.xml.

723 Dewey, R. K., and J. N. Moum, 1990: Enhancement of fronts by vertical mixing. *J. Geophys. Res.*,
724 **95 (C6)**, 9433–9445, https://doi.org/10.1029/JC095iC06p09433.

725 Durran, D. R., 1998: *Numerical Methods for Wave Equations in Geophysical Fluid Dynamics*.
726 Springer, 431–435 pp.

727 Ekman, V. W., 1905: On the influence of the Earth's rotation on ocean-currents. *Ark. Mat. Astron.*
728 *Fys.*, **2**, 1–53.

729 Elipot, S., R. Lumpkin, and G. Prieto, 2010: Modification of inertial oscillations by the mesoscale
730 eddy field. *Journal of Geophysical Research: Oceans*, **115 (C9)**, https://doi.org/https://doi.org/
731 10.1029/2009JC005679.

732 Fu, L.-L., 1981: Observations and models of inertial waves in the deep ocean. *Rev. Geophys.*,
733 **19 (1)**, 141–170, https://doi.org/10.1029/RG019i001p00141.

734 Furue, R., 2003: Energy transfer within the small-scale oceanic internal wave spectrum. *J. Phys.*
735 *Oceanogr.*, **33**, 267–282.

736 Furuichi, N., T. Hibiya, and Y. Niwa, 2005: Bispectral analysis of energy transfer within the
737 two-dimensional oceanic internal wave field. *J. Phys. Oceanogr.*, **35**, 2104–2109.

738 Furuichi, N., T. Hibiya, and Y. Niwa, 2008: Model-predicted distribution of wind-induced internal
739 wave energy in the world's oceans. *Journal of Geophysical Research: Oceans*, **113 (C9)**,
740 https://doi.org/https://doi.org/10.1029/2008JC004768.

741 Garrett, C., 2001: What is the "near-inertial" band and why is it different from the rest of the
742 internal wave spectrum? *J. Phys. Oceanogr.*, **31**, 962–971.

743 Garrett, C., and W. Munk, 1979: Internal waves in the ocean. *Annu. Rev. Fluid Mech.*, **11 (1)**,
744 339–369.

745 Gill, A. E., 1982: *Atmosphere-Ocean Dynamics*. Acad. Press, 662 pp.

746 Gill, A. E., 1984: On the behavior of internal waves in the wakes of storms. *J. Phys. Oceanogr.*,
747 **14**, 1129–1151.

748 Gregg, M. C., E. A. D'Asaro, T. J. Shay, and N. Larson, 1986: Observations of persistent mixing and
749 near-inertial internal waves. *Journal of Physical Oceanography*, **16 (5)**, 856–885, https://doi.org/
750 10.1175/1520-0485(1986)016⟨0856:OOPMAN⟩2.0.CO;2.

751 Grisouard, N., 2010: Réflexions et réfractions non-linéaires d'ondes de gravité internes. Ph.D.
752 thesis, Université de Grenoble, 224 pp.

753 Hinich, M. J., and C. S. Clay, 1968: The application of the Discrete Fourier Transform in the
754 estimation of power spectra, coherence, and bispectra of geophysical data. *Rev. Geophys.*, **6 (3)**,
755 347–363.

756 Hoskins, B. J., 1974: The role of potential vorticity in symmetric stability and instability. *Q. J. R.*
757 *Meteorol. Soc.*, **100 (425)**, 480–482, https://doi.org/10.1002/qj.49710042520.

758 Jiang, J., Y. Liu, and W. Perrie, 2005: Estimating the energy flux from the wind to ocean inertial
759 motions: The sensitivity to surface wind fields. *Geophys. Res. Lett.*, **32 L15610**, https://doi.org/
760 10.1029/2005GL023289.

761 Jones, W. L., 1967: Propagation of internal gravity waves in fluids with shear flow and rotation.
762 *Journal of Fluid Mechanics*, **30 (3)**, 439–448, https://doi.org/10.1017/S0022112067001521.

763 Joyce, T. M., J. M. Toole, P. Klein, and L. N. Thomas, 2013: A near-inertial mode observed
764 within a Gulf Stream warm-core ring. *J. Geophys. Res.*, **118 (4)**, 1797–1806, https://doi.org/
765 10.1002/jgrc.20141.

766 Kim, Y. C., and E. Powers, 1979: Digital bispectral analysis and its applications to nonlinear wave
767 interactions. *IEEE Trans. Plasma Sci.*, **7 (2)**, 120–131.

768 Klein, P., G. Lapeyre, and W. G. Large, 2004: Wind ringing of the ocean in presence of
769 mesoscale eddies. *Geophysical Research Letters*, **31 (15)**, https://doi.org/https://doi.org/10.1029/
770 2004GL020274.

771 Klein, P., and A. M. Treguier, 1993: Inertial resonance induced by an oceanic jet. *J. Phys.*
772 *Oceanogr.*, **23 (9)**, 1897–1915.

773 Klein, P., and A. M. Treguier, 1995: Dispersion of wind-induced inertial waves by a barotropic jet.
774 *J. Mar. Res.*, **53 (1)**, 1–22, https://doi.org/doi:10.1357/0022240953213331.

775 Klenz, T., H. L. Simmons, L. Centurioni, J. M. Lilly, J. J. Early, and V. Hormann, 2022: Esti-
776 mates of near-inertial wind power input using novel in situ wind measurements from minimet
777 surface drifters in the iceland basin. *Journal of Physical Oceanography*, **52 (10)**, 2417 – 2430,
778 https://doi.org/10.1175/JPO-D-21-0283.1.

779 Kunze, E., 1985: Near-inertial wave propagation in geostrophic shear. *J. Phys. Oceanogr.*, **15**,
780 544–565.

781 Kunze, E., 1986: The mean and near-inertial velocity fields in a warm-core ring. *J. Phys. Oceanogr.*,
782 **16 (8)**, 1444–1461.

783 Kunze, E., R.-C. Lien, C. B. Whalen, J. B. Girton, B. Ma, and M. C. Buijsman, 2023:
784 Seasonal variability of near-inertial/semidiurnal fluctuations and turbulence in the subarc-
785 tic north atlantic. *Journal of Physical Oceanography*, **53 (12)**, 2717–2735, https://doi.org/
786 10.1175/JPO-D-22-0231.1.

787 Kunze, E., and T. B. Sanford, 1984: Observations of near-inertial waves in a front. *J. Phys.*
788 *Oceanogr.*, **14**, 566—-581.

Kunze, E., R. W. Schmitt, and J. M. Toole, 1995: The energy balance in a warm-core ring's near-inertial critical layer. *J. Phys. Oceanogr.*, **25**, 942–957.

Kunze, E., and J. M. Toole, 1997: Tidally-driven vorticity, diurnal shear and turbulence atop Fieberling Seamount. *J. Phys. Oceanogr.*, **27**, 2663–2693.

Kunze, E., A. J. Williams III, and M. G. Briscoe, 1990: Observations of shear and vertical stability from a neutrally buoyant float. *Journal of Geophysical Research: Oceans*, **95 (C10)**, 18 127–18 142, https://doi.org/https://doi.org/10.1029/JC095iC10p18127.

Leaman, K. D., 1976: Observations on the vertical polarization and energy flux of near-inertial waves. *J. Phys. Oceanogr.*, **6 (6)**, 894–908.

Leaman, K. D., and T. B. Sanford, 1975: Vertical energy propagation of inertial waves: A vector spectral analysis of velocity profiles. *J. Geophys. Res.*, **80 (15)**, 1975–1978, https://doi.org/10.1029/JC080i015p01975.

Lee, D.-K., and P. P. Niiler, 1998: The inertial chimney: The near-inertial energy drainage from the ocean surface to the deep layer. *J. Geophys. Res.*, **103 (C4)**, 7579–7591, https://doi.org/10.1029/97JC03200.

Lelong, M.-P., P. Bouruet-Aubertot, and Y. Cuypers, 2016: Near-inertial energy propagation inside a Mediterranean anticyclonic eddy. *J. Phys. Oceanogr.*

Llewellyn Smith, S. G., 1999: Near-inertial oscillations of a barotropic vortex: Trapped modes and time evolution. *Journal of Physical Oceanography*, **29 (4)**, 747 – 761, https://doi.org/10.1175/1520-0485(1999)029⟨0747:NIOOAB⟩2.0.CO;2, URL https://journals.ametsoc.org/view/journals/phoc/29/4/1520-0485_1999_029_0747_niooab_2.0.co_2.xml.

Lueck, R., and T. Osborn, 1986: The dissipation of kinetic energy in a warm-core ring. *J. Geophys. Res.*, **91 (C1)**, 803–818, https://doi.org/10.1029/JC091iC01p00803.

MacKinnon, J. A., M. H. Alford, R. Pinkel, J. Klymak, and Z. Zhao, 2013: The latitudinal dependence of shear and mixing in the Pacific transiting the critical latitude for PSI. *J. Phys. Oceanogr.*, **43**, 3–16.

Mahadevan, A., 2006: Modeling vertical motion at ocean fronts: Are nonhydrostatic effects relevant at submesoscales? *Ocean Model.*, **14 (3–4)**, 222–240.

Mahadevan, A., J. Oliger, and R. Street, 1996a: A nonhydrostatic mesoscale ocean model. Part I: Well-posedness and scaling. *J. Phys. Oceanogr.*, **26**, 1868–1880.

Mahadevan, A., J. Oliger, and R. Street, 1996b: A nonhydrostatic mesoscale ocean model. Part II: Numerical implementation. *J. Phys. Oceanogr.*, **26**, 1881–1900.

Martínez-Marrero, A., and Coauthors, 2019: Near-inertial wave trapping near the base of an anticyclonic mesoscale eddy under normal atmospheric conditions. *Journal of Geophysical Research: Oceans*, **124 (11)**, 8455–8467, https://doi.org/https://doi.org/10.1029/2019JC015168.

McComas, C., and F. Bretherton, 1977: Resonant interaction of oceanic internal waves. *J. Geophys. Res.*, **82 (9)**, 1397–1412, https://doi.org/10.1029/JC082i009p01397.

McComas, C., and M. Briscoe, 1980: Bispectra of internal waves. *J. Fluid Mech.*, **97**, 205–213, https://doi.org/10.1017/S0022112080002510.

Mooers, C. N. K., 1975a: Several effects of a baroclinic current on the cross-stream propagation of inertial-internal waves. *Geophys. Fluid Dyn.*, **6**, 245–275.

Mooers, C. N. K., 1975b: Several effects of baroclinic currents on the three-dimensional propagation of inertial-internal waves. *Geophys. Fluid Dyn.*, **6**, 277–284.

Nagai, T., A. Tandon, E. Kunze, and A. Mahadevan, 2015: Spontaneous generation of near-inertial waves by the Kuroshio Front. *J. Phys. Oceanogr.*, **in press**, https://doi.org/10.1175/JPO-D-14-0086.1.

Naveira Garabato, A. C., X. Yu, J. Callies, R. Barkan, K. L. Polzin, E. E. Frajka-Williams, C. E. Buckingham, and S. M. Griffies, 2022: Kinetic energy transfers between mesoscale and submesoscale motions in the open ocean's upper layers. *Journal of Physical Oceanography*, **52 (1)**, 75–97, https://doi.org/10.1175/JPO-D-21-0099.1.

Niwa, Y., and T. Hibiya, 1997: Nonlinear processes of energy transfer from traveling hurricanes to the deep ocean internal wave field. *J. Geophys. Res.*, **102 (C6)**, 12 469–12 477, https://doi.org/10.1029/97JC00588.

Niwa, Y., and T. Hibiya, 1999: Response of the deep ocean internal wave field to traveling midlatitude storms as observed in long-term current measurements. *J. Geophys. Res.*, **104 (C5)**, 10 981–10 989.

Pallàs-Sanz, E., J. Candela, J. Sheinbaum, J. Ochoa, and J. Jouanno, 2016: Trapping of the near-inertial wave wakes of two consecutive hurricanes in the Loop Current. *J. Geophys. Res.*, **121 (10)**, 7431–7454, https://doi.org/10.1002/2015JC011592.

Perkins, H., 1976: Observed effect of an eddy on inertial oscillations. *Deep-Sea Res.*, **23**, 1037–1042.

Plueddemann, A., and J. Farrar, 2006: Observations and models of the energy flux from the wind to mixed-layer inertial currents. *Deep Sea Research Part II: Topical Studies in Oceanography*, **53 (1)**, 5–30, https://doi.org/https://doi.org/10.1016/j.dsr2.2005.10.017, ocean Mixing.

Polzin, K., 1996: Statistics of the richardson number: Mixing models and finestructure. *Journal of Physical Oceanography*, **26 (8)**, 1409 – 1425, https://doi.org/10.1175/1520-0485(1996)026⟨1409:SOTRNM⟩2.0.CO;2, URL https://journals.ametsoc.org/view/journals/phoc/26/8/1520-0485_1996_026_1409_sotrnm_2_0_co_2.xml.

Polzin, K. L., and Y. V. Lvov, 2011: Toward regional characterizations of the oceanic internal wavefield. *Rev. Geophys.*, **49 (4)**, n/a–n/a, https://doi.org/10.1029/2010RG000329, rG4003.

Raja, K. J., M. C. Buijsman, J. F. Shriver, B. K. Arbic, and O. Siyanbola, 2022: Near-inertial wave energetics modulated by background flows in a global model simulation. *Journal of Physical Oceanography*, **52 (5)**, 823–840, https://doi.org/10.1175/JPO-D-21-0130.1.

Rimac, A., J.-S. von Storch, C. Eden, and H. Haak, 2013: The influence of high-resolution wind stress field on the power input to near-inertial motions in the ocean. *Geophysical Research Letters*, **40 (18)**, 4882–4886, https://doi.org/https://doi.org/10.1002/grl.50929.

Silverthorne, K. E., 2010: Near-inertial and thermal upper ocean response to atmospheric forcing in the North Atlantic Ocean. Ph.D. thesis, MIT/WHOI, 135 pp.

Silverthorne, K. E., and J. M. Toole, 2009: Seasonal kinetic energy variability of near-inertial motions. *J. Phys. Oceanogr.*, **39**, 1035—-1049.

Skitka, J., B. K. Arbic, R. Thakur, D. Menemenlis, W. R. Peltier, Y. Pan, K. Momeni, and Y. Ma, 2024: Probing the nonlinear interactions of supertidal internal waves using a high-resolution regional ocean model. *Journal of Physical Oceanography*, **54 (2)**, 399 – 425, https://doi.org/10.1175/JPO-D-22-0236.1, URL https://journals.ametsoc.org/view/journals/phoc/54/2/JPO-D-22-0236.1.xml.

Sun, O., and R. Pinkel, 2012: Energy transfer from high-shear, low-frequency internal waves to high-frequency waves near Kaena Ridge, Hawaii. *J. Phys. Oceanogr.*, **42**, 1524–1547.

Sun, O., and R. Pinkel, 2013: Subharmonic energy transfer from the semidiurnal internal tide to near-diurnal motions over Kaena Ridge, Hawaii. *J. Phys. Oceanogr.*, **43**, 766–789.

Swami, A., J. M. Mendel, and C. L. Nikias, 2014: Higher-order spectral analysis toolbox for use with matlab. MATLAB Central File Exchange, URL https://www.mathworks.com/matlabcentral/fileexchange/3013-hosa-higher-order-spectral-analysis-toolbox.

Thomas, L. N., L. Rainville, O. Asselin, W. R. Young, J. Girton, C. B. Whalen, L. Centurioni, and V. Hormann, 2020: Direct observations of near-inertial wave ζ-refraction in a dipole vortex. *Geophysical Research Letters*, **47 (21)**, e2020GL090 375, https://doi.org/https://doi.org/10.1029/2020GL090375, e2020GL090375 10.1029/2020GL090375.

van Meurs, P., 1998: Interactions between near-inertial mixed layer currents and the mesoscale: The importance of spatial variabilities in the vorticity field. *Journal of Physical Oceanography*, **28 (7)**, 1363–1388, https://doi.org/10.1175/1520-0485(1998)028⟨1363:IBNIML⟩2.0.CO;2.

Wang, D.-P., 1991: Generation and propagation of inertial waves in the subtropical front. *J. Mar. Res.*, **49 (4)**, 619–633.

Weller, R. A., 1982: The relation of near-inertial motions observed in the mixed layer during the JASIN (1978) experiment to the local wind stress and to quasi-geostrophic flow field. *J. Phys. Oceanogr.*, **12**, 1122–1136.

Weller, R. A., 1985: Near-surface velocity variability at inertial and subinertial frequencies in the vicinity of the california current. *Journal of Physical Oceanography*, **15 (4)**, 372 – 385, https://doi.org/10.1175/1520-0485(1985)015⟨0372:NSVVAI⟩2.0.CO;2.

Whitt, D. B., and L. N. Thomas, 2013: Near-inertial waves in strongly baroclinic currents. *J. Phys. Oceanogr.*, **43**, 706–725.

Williams, E. F., E. Kunze, and J. A. MacKinnon, 2006: Bispectra of internal tides and parametric subharmonic instability. M.S. thesis, School of Oceanography, University of Washington, 26 pp.

Winters, K. B., M. Claret, M.-P. Lelong, and Y. Ourmières, 2024: A pressure projection scheme with near-spectral accuracy for nonhydrostatic flow in domains with open boundaries. *Journal of Advances in Modeling Earth Systems*, **16 (6)**, e2023MS004 040, https://doi.org/https://doi.org/10.1029/2023MS004040.

Winters, K. B., J. A. MacKinnon, and B. Mills, 2004: A spectral model for process studies of rotating, density-stratified flows. *J. Atmos. Oceanic Technol.*, **21**, 69–94.

Wu, Y., and Y. Pan, 2023: Energy cascade in the garrett–munk spectrum of internal gravity waves. *Journal of Fluid Mechanics*, **975**, A11, https://doi.org/10.1017/jfm.2023.862.

Young, W. R., and M. Ben Jelloul, 1997: Propagation of near-inertial oscillations through a geostrophic flow. *J. Mar. Res.*, **55**, 735–766.

Zhai, X., R. J. Greatbatch, and J. Zhao, 2005: Enhanced vertical propagation of storm-induced near-inertial energy in an eddying ocean channel model. *Geophysical Research Letters*, **32 (18)**, https://doi.org/https://doi.org/10.1029/2005GL023643.

Zhang, K. Q., and J. Marotzke, 1999: The importance of open-boundary estimation for an Indian Ocean GCM-data synthesis. *J. Mar. Res.*, **57 (2)**, 305–334.